The relationship between stratabound Pb–Zn–Ag and porphyry–skarn Mo mineralization in the Laochang deposit, southwestern China: Constraints from pyrite Re-Os isotope, sulfur isotope, and trace element data

Yu-Miao Meng[a], Rui-Zhong Hu[a,b,*], Xiao-Wen Huang[a], Jian-Feng Gao[a], Liang Qi[a], Chuan Lyu[a,b]

[a] State Key Laboratory of Ore Deposit Geochemistry, Institute of Geochemistry, Chinese Academy of Sciences, Guiyang 550081, China
[b] University of Chinese Academy of Sciences, Beijing 100049, China

ARTICLE INFO

ABSTRACT

The Laochang polymetallic deposit is located in the Sanjiang Tethyan metallogenic province of southwestern China. This deposit contains stratabound (and locally vein-type) Pb–Zn–Ag mineralization and underlying porphyry–skarn Mo mineralization. The stratabound Pb–Zn–Ag mineralization is characterized by massive sulfide ores composed mainly of pyrite, sphalerite, galena, and minor chalcopyrite, whereas the underlying porphyry–skarn Mo mineralization is characterized by quartz–sulfide veins comprising mainly pyrite, chalco-pyrite, molybdenite, and minor sphalerite and galena. The age and origin of the stratabound Pb–Zn–Ag mineralization has long been debated, and its relationship to the porphyry–skarn Mo mineralization remains un-known. Integrated pyrite Re-Os isotope, sulfur isotope, and in situ trace element data are used here to constrain the age and origin of both types of mineralization and their genetic relationships.

Pyrite related to porphyry–skarn Mo mineralization yields a Re-Os isochron age of 47.3 ± 4.8 Ma, which is consistent with a previous molybdenite Re-Os age of the quartz–sulfide ores and zircon U-Pb ages of the granite porphyry (~44–50 Ma). Pyrite from the stratabound Pb–Zn–Ag mineralization failed to yield a geologically meaningful age, but associated sphalerite and galena have a Re-Os isochron age of 308 ± 25 Ma (Liu et al., 2015), which is consistent with the Carboniferous age of the host basalts. Pyrite, sphalerite, galena, and chal-copyrite from the stratabound Pb–Zn–Ag mineralization have $\delta^{34}S$ values (−2.1 to 0.5‰; average 0.48‰) indistinguishable from those of sulfides from the porphyry–skarn Mo mineralization (−4 to 1.9‰; average 0.52‰). Initial Os isotope ratios indicate a mainly crustal origin for both types of mineralization. The calculated $(Se/S)_{fluid}$ and Co/Ni values of pyrite from the stratabound Pb–Zn–Ag mineralization indicate a mixed sedi-mentary and hydrothermal origin, with a significant magmatic contribution. The identification of a magmatic component, Eocene sulfide mineralization, and phyllic and propylitization alteration in stratabound Pb–Zn–Ag ores indicates that the magmatic–hydrothermal component reflects the overprinting of Carboniferous volcano-genic massive sulfide mineralization by magmatic–hydrothermal fluids derived from an Eocene granite por-phyry.

1. Introduction

The Sanjiang Tethyan metallogenic province (STMP) in the eastern Tibetan Plateau is an important part of the giant eastern Tethyan metallogenic belt (Fig. 1a; Hou et al., 2007). Numerous porphyry Cu, Cu-Mo, and Cu-Au deposits define two sub-parallel porphyry belts in the STMP (Fig. 1a; Hou et al., 2006; Deng et al., 2014; Mao et al., 2014). These porphyry deposits are dated at 33–40 Ma (molybdenite Re-Os age) and are related to India–Eurasia continental collision (Wang et al., 2005; Hou et al., 2006; Deng et al., 2014). To the southwest of the two

porphyry zones, numerous stratabound and minor vein and metasomatic polymetallic deposits occur within the Changning–Menglian back-arc basin (CMBB), including the Laochang Pb–Zn–Ag, Tongchangjie Cu, and Dapingzhang Cu-Zn deposits (Zaw et al., 2007; Wang et al., 2010). Recent exploration at the Laochang deposit has revealed porphyry–skarn Mo mineralization is underlying the stratabound Pb–Zn–Ag orebodies. This discovery has led to more controversy over the origin of the Laochang deposit because of the unknown relationship between the two types of mineralization. Two contrasting viewpoints have been proposed for the formation of the stratabound Pb–Zn–Ag
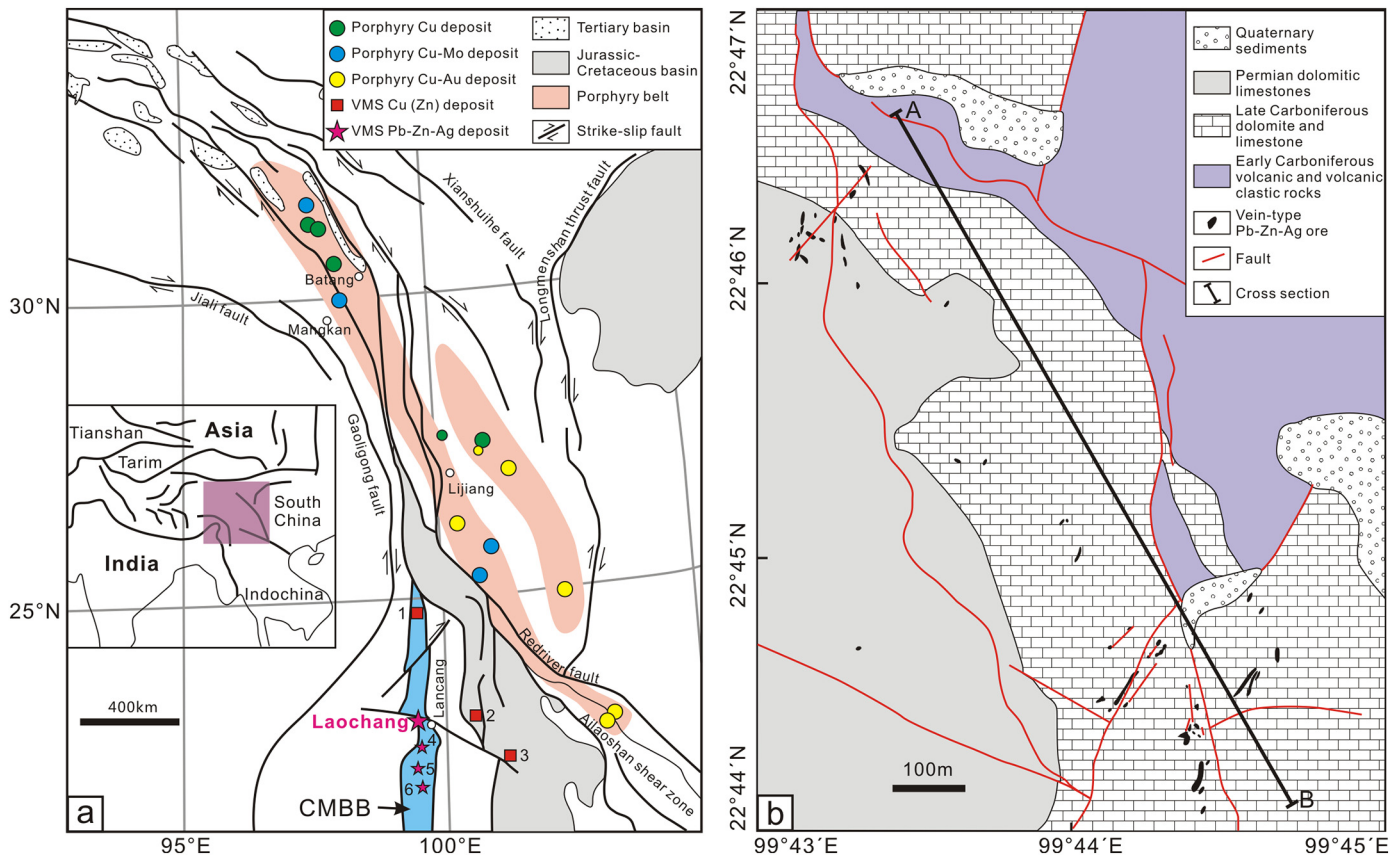
Fig. 1. (a) Simplified geological map showing the tectonic framework of the Sanjiang Tethyan metallogenic province and the distribution of Pb–Zn–Ag and porphyry deposits. Numbers 1, 2, and 3 represent the Tongchangjie, Dapingzhang, and Sandashan Cu ± Zn ± Pb polymetallic deposits, respectively, whereas 4, 5, and 6 represent the smaller Bansha, Nanya, and Padi Pb–Zn–Ag deposits, respectively. (b) Geological map of the Laochang deposit showing the distribution of orebodies and location of the cross-section in Fig. 2 (after Li et al., 2010a). CMBB = Changning–Menglian back-arc basin.

mineralization. Some studies have argued that the stratabound Pb–Zn–Ag mineralization is typical volcanogenic massive sulfide mineralization that is independent of porphyry system (Li et al., 1996; Wang et al., 1997; Li et al., 2009b, 2010a; Yang, 2014; Liu et al., 2015), whereas others have considered the mineralization to be a product of a common magmatic–hydrothermal system related to Eocene granitic intrusions (Ouyang and Xu, 1991; Xu and Ouyang, 1991; X.-D. Deng et al., 2016), because distal carbonate-replacement Pb–Zn–Ag deposits can form around intrusion-centered porphyry Cu system (Sillitoe, 2010). The former viewpoint is based mainly on the different mineralization styles, ages, fluid sources, and lack of a clear contact relationship between the two types of mineralization. The latter model is based on the high Cu contents, magma-dominated ore-forming fluids of the stratabound Pb–Zn–Ag ores (Ouyang and Xu, 1991; Xu and Ouyang, 1991), and similar ages (~46 Ma, Long et al., 2008; X.-D. Deng et al., 2016) of the stratabound Pb–Zn–Ag mineralization and granite porphyry. However, due to unknown sample detail, the ~46 Ma sphalerite Rb-Sr age reported by Long et al. (2008) cannot be evaluated. X.-D. Deng et al. (2016) reported ~46 Ma Re-Os isochron age for pyrite from the stratabound Pb–Zn–Ag mineralization. Lacking of other geochemical data to determine the origin of pyrite makes the meaning of pyrite Re-Os age ambiguous. Therefore, the timing and origin of stratabound Pb–Zn–Ag mineralization in the Laochang deposit has been debated and thus its relationship to porphyry–skarn Mo mineralization remains controversial, which limits our understanding of the Laochang hydrothermal system and sulfide mineralization in the STMP.

Conditions of ore forming processes can be reconstructed from trace element and isotope compositions of sulfides. Re-Os dating of sulfides such as pyrite, arsenopyrite, and chalcopyrite has proven to be a robust and direct tool for constraining the age of ore mineralization (e.g., Stein

et al., 2000; Mathur et al., 2002; Morelli et al., 2004; Morelli and Creaser, 2006; Selby et al., 2009; Huang et al., 2013a, 2013b, 2013c; Hnatyshin et al., 2015; X.-H Deng et al., 2016, Li et al., 2016; Kelley et al., 2017). Initial Os isotope ratios can also be used to trace the source of Os and, by inference, the metals within the sulfide minerals (e.g., Mathur et al., 2000, 2002; Barra et al., 2017). Sulfur isotope studies of sulfides can also be used to infer the sulfur source(s) of ore-forming fluids (e.g., Sakai, 1968). Pyrite, the most common sulfide, can record changes in fluid chemistry during the evolution of the fluid from which it precipitated (Cook et al., 2009; Reich et al., 2013, 2016; Gregory et al., 2014, 2016; Ingham et al., 2014; Tanner et al., 2016; Tardani et al., 2017). Pyrite is characterized by variable trace element compositions in a variety of mineral deposits (Deditius et al., 2008, 2013; Large et al., 2009, 2015; Zwahlen et al., 2014; Revan et al., 2014; Genna and Gaboury, 2015; Gadd et al., 2016; Mukherjee and Large, 2017). Thus, trace element geochemistry of pyrite can be used to trace the fluid source(s). For example, the Co/Ni and Se/S ratios of pyrite are very powerful in discriminating their origins (e.g., Bajwah et al., 1987; Huston et al., 1995a, 1995b; Layton-Matthews et al., 2005; Gregory et al., 2015).

Here we present an integrated study of Re-Os isotopes, sulfur isotopes, and in situ trace elements in pyrite from the stratabound Pb–Zn–Ag and porphyry–skarn Mo mineralization from the Laochang deposit. Combined with previous data (Li et al., 1995, 2015; Zhao et al., 2012; Liang, 2014), this new dataset is used to constrain the timing, origin, and relationships of these two types of mineralization.

2. Geological background

The STMP is composed of a mosaic of accreted terranes and blocks

(Mo et al., 1993; Burchfiel and Chen, 2012; Metcalfe, 2013). The complex geological and tectonic history of the STMP involves subduction of the Tethyan Ocean slab, subsequent orogenesis by arc–continent collision during the Paleozoic to Mesozoic, and continent–continent collision during the Eocene (Mo et al., 1993; Yin and Harrison, 2000; Metcalfe, 2013). The CMBB in the southwest of the STMP was formed by an amalgamation of four continental blocks (the South China, Simao, Baoshan, and Tengchong blocks) in the Late Triassic during the closure of the Paleo-Tethys Ocean (Metcalfe, 2013). The western margin of the CMBB is mainly composed of Paleozoic sedimentary and volcanic rocks. The sedimentary rocks include the Devonian chert, sandstone and shale, and Late Carboniferous to Early Permian dolomite and dolomitic limestone. In the northern part of the CMBB, volcanic rocks consist mainly of Early Silurian Nantinghe gabbro and meta-basalt (Wang et al., 2013), early Carboniferous Gengma meta-basalt (Yang, 2014), and Late Permian Damangguanfang basalt (Jian et al., 2009). In the southern part of the CMS, volcanic rocks are dominated by the early Carboniferous Yiliu Group (Yang, 2014), which has a zircon U-Pb age of 324 ± 3 Ma (Chen et al., 2010).

The Laochang deposit in the CMBB is composed of two types of mineralization: the stratabound and vein-type Pb–Zn–Ag mineralization and porphyry-skarn Mo mineralization. The stratabound and vein-type mineralization has a proven reserve of 1737 t Ag (average grade 222 g/t), 0.51 Mt. Pb (5.1 wt%), 0.34 Mt. Zn (3.1 wt%), and 0.1 Mt. Cu (0.2 wt%) (Li et al., 2010b). Underlying the Pb–Zn–Ag orebodies, there is a porphyry–skarn Mo resource containing 117,800 t Mo with an average grade of 0.15 wt% (Li et al., 2010b). The Laochang Pb–Zn–Ag

mineralization is hosted by early Carboniferous volcanic rocks and late Carboniferous to early Permian marine carbonate rocks (Fig. 1b and 2).

Five types of sulfide mineralization are present in the Laochang deposit: vein-type Pb–Zn–Ag (~1500–1800 m elevation), stratabound Pb–Zn–Ag (~1200–1700 m), stratabound Cu-bearing Pb–Zn–Ag (~1200–1650 m), skarn Mo (~800–1200 m), and porphyry Mo stockwork (< 1000 m) mineralization (Fig. 2; Li et al., 2010b). The vein-type Pb–Zn–Ag mineralization is hosted mainly by late Carboniferous limestone (Fig. 1b and 2). These veins are 0.3 to 15 m wide and have grades of 1.8–20.3 wt% Pb, 1.4–8.9 wt% Zn, and 96–635 g/t Ag (Li et al., 2010b). Hydrothermal alteration around these veins is dominated by calcite, ankerite, and rhodochrosite. The stratabound Pb–Zn–Ag and Cu-bearing Pb–Zn–Ag orebodies are hosted by early Carboniferous volcanic rocks and have similar Pb, Zn, and Ag grades of 0.2–10 wt%, 0.4–5.0 wt%, and 20–200 g/t, respectively (Li et al., 2010b). The Cu-bearing Pb–Zn–Ag ores have Cu contents of 0.1 to 2.2 wt%. The volcanic rocks hosting the stratabound Pb–Zn–Ag ores are characterized by propylitic alteration with a mineral assemblage of epidote, chlorite, calcite, and kaolinite, whereas those of the Cu-bearing ores are dominated by phyllic alteration assemblages of sericite and quartz. Both types of ore contain pyrite, galena, sphalerite, and chalcopyrite, with minor arsenopyrite, pyrrhotite, argentite, and native silver. The vein-type Pb–Zn–Ag mineralization is considered to be derived from or overprinted by porphyry hydrothermal fluids, whereas stratabound mineralization belongs to VMS system (Yang, 2014).

Skarn Mo mineralization occurs mainly along the contact zones between the late Carboniferous trachyandesite and Eocene granitic
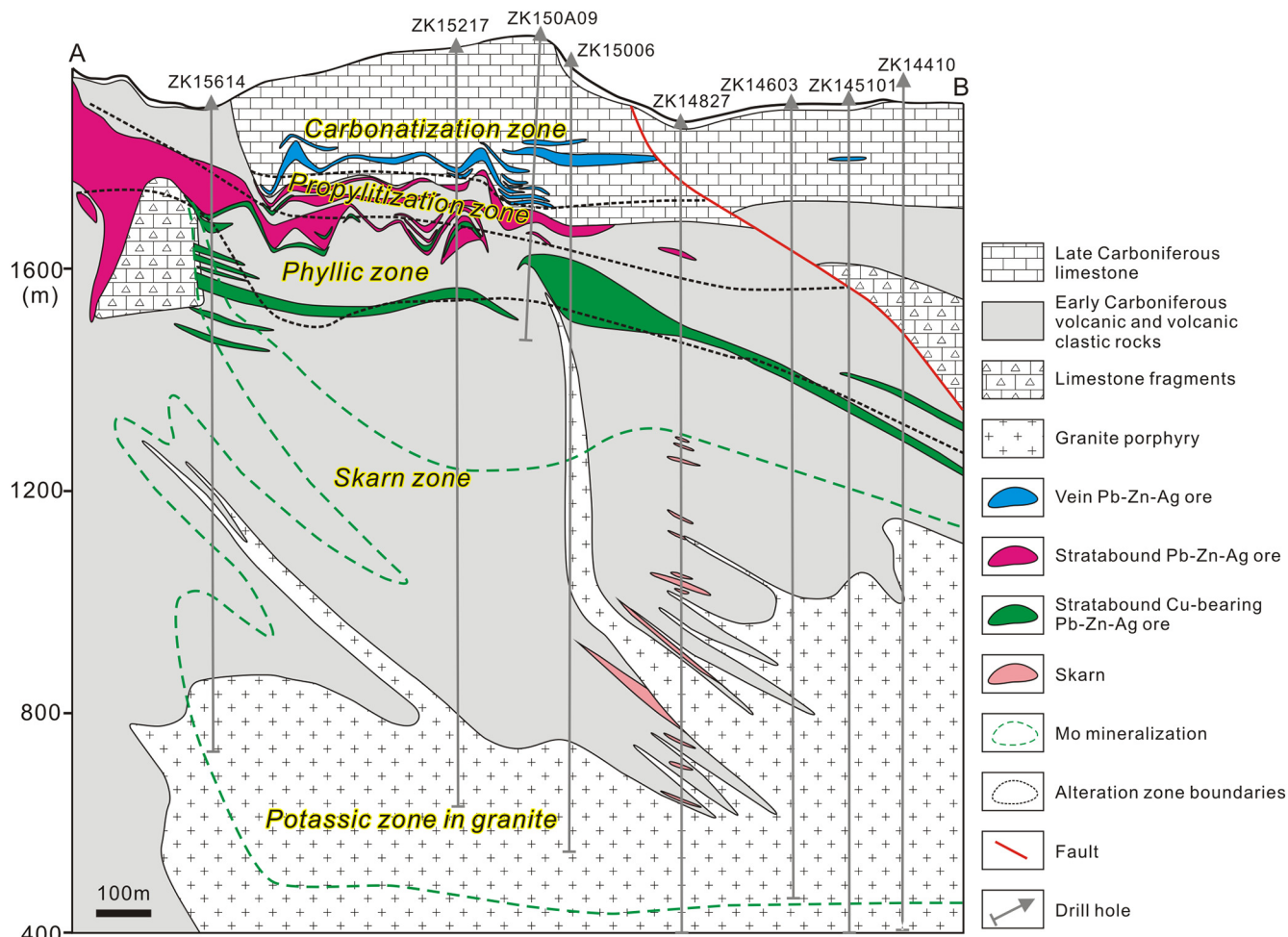

Fig. 2. Cross-section of the Laochang deposit along the strike of the orebodies, showing alteration zones, mineralization types, and the distribution of orebodies (modified from X.-D. Deng et al., 2016).
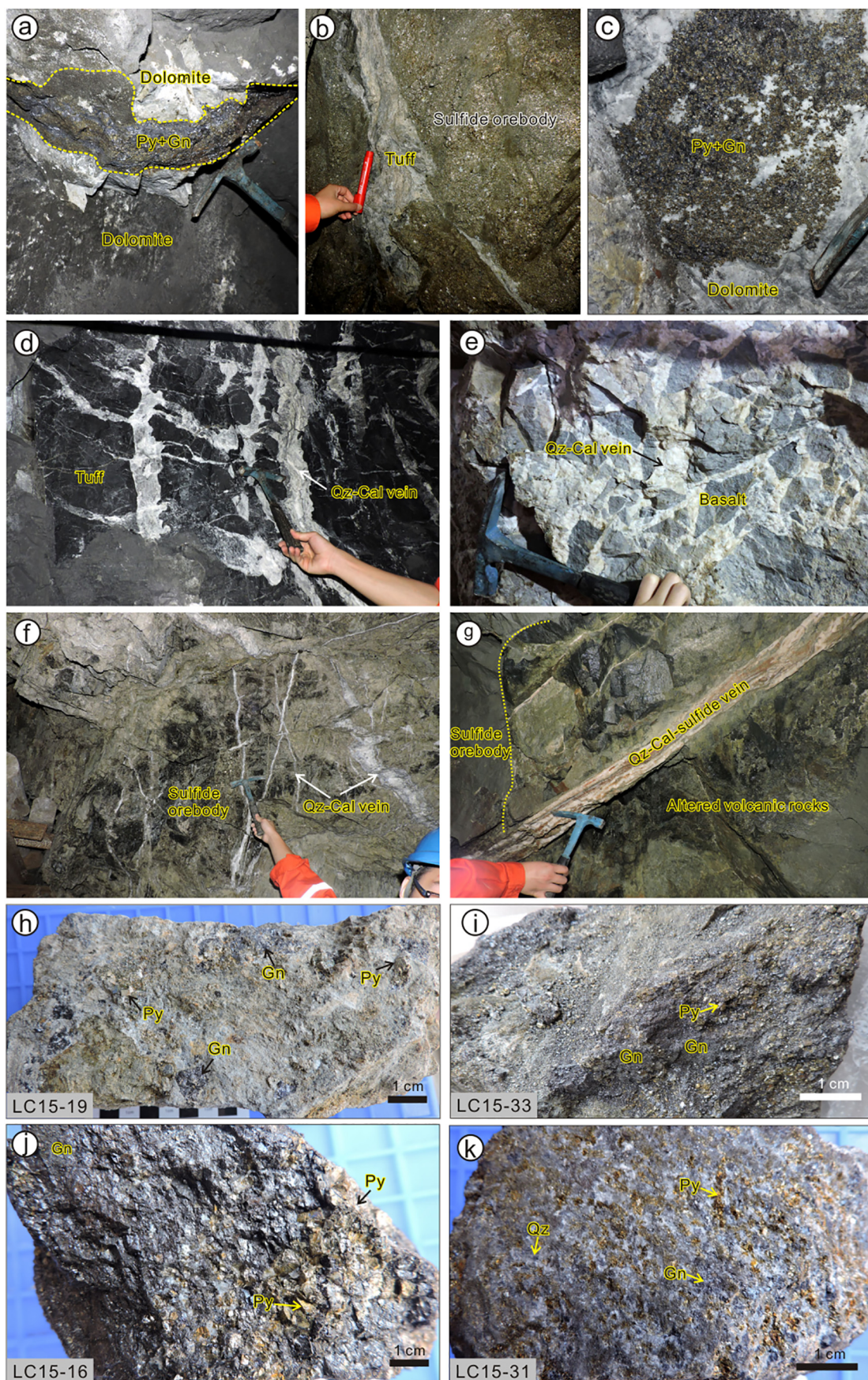
(caption on next page)

Fig. 3. Outcrop and ore photographs showing the stratabound Pb–Zn–Ag mineralization in the Laochang deposit. (a) Sulfide vein in host dolomite composed of pyrite, galena, and minor sphalerite (1480 m mining tunnel). Minor dolomite breccia enclosed in massive sulfides. (b) Sulfide orebody in the 1650 m mining tunnel containing tuff breccia, indicating that pyrite formed later than the tuff. Sulfides are mainly fine-grained pyrite and locally chalcopyrite. The tuff has been deformed and is nearly entirely altered to clay. (c) Disseminated pyrite and galena in dolomite (1480 m mining tunnel). (d) Tuff adjacent to sulfide orebody crosscut by quartz-calcite veins (1480 m mining tunnel), forming network structure. (e) Basalt around sulfide orebody crosscut by quartz-calcite veins to form breccia structure (1480 m mining tunnel). (f) Massive sulfide orebody hosted in tuffaceous volcanic rocks crosscut by quartz-calcite veins with various widths (1480 m mining tunnel). (g) Both altered volcanic rocks and sulfide orebody crosscut by quartz-calcite-sulfide veins (1480 m mining tunnel). (h) Disseminated ores showing euhedral pyrite and anhedral galena in tuff (LC15-19). (i) Massive ores composed of subhedral to euhedral pyrite and subhedral galena (LC15-33). (j) Massive ore consisting of euhedral pyrite and galena. The surface of pyrite is partly oxidized (LC15-16). (k) Massive ore composed mainly of subhedral to anhedral pyrite, galena, and quartz (LC15-31). Mineral abbreviations: *Py* = pyrite; *Gn* = galena; *Qz* = quartz; *Cal* = calcite.

porphyry (Fig. 2). The skarn assemblages include diopside, garnet, epidote, actinolite, tremolite, and chlorite. The main sulfide minerals include molybdenite, chalcopyrite, pyrite, and pyrrhotite, which are accompanied by minor amounts of scheelite and cassiterite. Porphyry Mo mineralization is hosted by the granitic porphyry and is characterized by quartz–sulfide veins, stockworks, and dense to sparse sulfide disseminations in altered granite, all mostly at depths of > 800 m (Fig. 2). The hydrothermal alteration is dominated by K-feldspar, sericite, and quartz (Fig. 2). Molybdenite is commonly intergrown with pyrite, chalcopyrite, and arsenopyrite.

3. Sample descriptions

Samples representing the stratabound Pb–Zn–Ag mineralization (including Cu-bearing and Cu-barren samples) were collected from mining adits between 1480 and 1895 m elevation (Fig. 3a–g). A detailed description of each sample is provided in Appendix A. Sulfides (pyrite ± galena) occur as veins in dolomite or as massive aggregates associated with tuff (Fig. 3a–b). Pyrite and galena are also found disseminated in dolomite and tuff (Fig. 3c, h). Numerous quartz-calcite ± sulfide veins crosscut the tuff, basalt or altered volcanic rocks (Fig. 3d–g), and locally also the stratabound sulfide orebodies (Fig. 3f–g). The stratabound ores are mainly massive and are composed of pyrite, galena, sphalerite, chalcopyrite, and minor quartz, calcite, kaolinite, K-feldspar, and rutile (Figs. 3i–k and 4). Two types of pyrite were identified in all types of stratabound ore: pyrite nodules composed of microcrystalline pyrite (Fig. 4a), and anhedral–subhedral to euhedral pyrite (Fig. 4b–d). Pyrite nodules were not analyzed due to numerous silicate intergrowths and the small grain size of the nodule pyrite relative to the laser ablation spot size (40 μm). Fractures in euhedral pyrite are typically filled by chalcopyrite that has been crosscut by later calcite veinlets (Fig. 4b). Sphalerite and galena commonly replace pyrite along its margins (Fig. 4c–d). The crosscutting relationships indicate that pyrite formed earlier than chalcopyrite, sphalerite, and galena. Some samples show different pyrite generations at the thin section scale. Sample LC15-19 contains early pyrite grains within tuff and later pyrite grains within galena (Fig. 4e–g). Sample LC15-21 contains early coarse-grained and late fine-grained pyrite (Fig. 4h–j).

Samples of porphyry–skarn Mo mineralization were collected from the mining section at 1480 m elevation (Fig. 5a–b) in the Laochang deposit. Ores include banded, vein, and stockwork types. Banded ore is composed of interbedded dark skarn and light limestone (Fig. 5a). Pyrite and chalcopyrite are disseminated in the skarn or occur in veins crosscutting skarn and limestone (Fig. 5a). Vein and stockwork ores are composed of pyrite ± molybdenite ± quartz veins crosscutting skarn (Fig. 5b–d). Different types of ore from the porphyry-skarn mineralization have a similar mineral assemblage comprising variable amounts of pyrite, molybdenite, chalcopyrite, andradite, diopside, quartz, and calcite (Fig. 5).

Detailed descriptions of the mineral assemblages and paragenetic sequences of the stratabound Pb–Zn–Ag and porphyry–skarn mineralization are shown in Fig. 6 (Yang, 2014). The stratabound Pb–Zn–Ag mineralization is divided into two stages. Early stage stratabound Pb–Zn–Ag mineralization consists of colloidal pyrite, pyrite, chalcopyrite, and minor galena, sphalerite, marcasite, and pyrrhotite, whereas

late-stage stratabound Pb–Zn–Ag mineralization is characterized by pyrite, galena, sphalerite, and minor marcasite, pyrrhotite, argentite, and native silver (Fig. 6). Epidote, chlorite, quartz, and calcite are common in both stages. According to the mineral assemblages containing large amounts of galena and sphalerite, pyrite from the stratabound Pb–Zn–Ag ores in this study is mainly from the late-stage stratabound Pb–Zn–Ag mineralization (Fig. 6). The porphyry–skarn Mo mineralization can be divided into five stages: skarn, quartz, early sulfide, late sulfide, and carbonate (Fig. 6). The skarn stage is characterized by a mineral assemblage of diopside, garnet, vesuvianite, epidote, actinolite, chlorite, and minor pyrite, arsenopyrite, molybdenite, scheelite, and cassiterite (Fig. 6). The quartz stage is composed mainly of quartz or quartz–chalcopyrite veins. The early sulfide stage is characterized by pyrite, chalcopyrite, molybdenite, quartz, and minor arsenopyrite and bismuthinite, and the late sulfide stage consists of pyrite, galena, sphalerite, quartz, sericite, and minor argentite, native silver, lillianite, chiviatite, and stibnite (Fig. 6). The carbonate stage is characterized by calcite and fluorite veins. According to crosscutting relationships (quartz–sulfide veins cutting skarn) and mineral assemblages (absence of galena and sphalerite) (Fig. 5), pyrite from the porphyry-skarn ores in this study belongs to the early sulfide stage of porphyry-skarn Mo mineralization (Fig. 6).

4. Analytical methods

Pyrite separates used for Re-Os and sulfur isotope analyses were acquired by conventional mineral separation methods (Huang et al., 2013b). Selected samples were first crushed in a stainless-steel bowl and then sieved to a size of ~250 μm. Samples were then handpicked under a binocular microscope to obtain high-purity pyrite separates. Trace element analyses of pyrite by laser ablation–inductively coupled plasma–mass spectrometry (LA–ICP–MS) were performed on polished thin sections with a thickness of ~100 μm. Prior to LA–ICP–MS analyses, detailed observations of pyrite textures, grain sizes, and associated minerals were carried out using optical and scanning electron microscopy. This allowed the different pyrite generations to be identified, a suitable laser ablation spot size to be chosen, and inclusions and areas of zoning in the pyrite to be avoided during analysis.

4.1. Re-Os isotope analysis

Re and Os isotopes were analyzed using a PE ELAN DRC-e ICP–MS at the State Key Laboratory of Ore Deposit Geochemistry, Institute of Geochemistry, Chinese Academy of Sciences (SKLODG, IGCAS), Guiyang, China. The detailed analytical procedures are described by Qi et al. (2010, 2013). For samples with relatively high Re contents (> 5 ppb), ca. 0.5 g of pyrite was weighed and loaded into a 200 ml Carius tube with known amounts of ^{185}Re and ^{190}Os spikes. Samples were then digested and equilibrated in 10 ml of concentrated HNO_3 and 2 ml of HCl at 200 °C for ca. 12 h. To improve the signal intensities of Re and Os, ca. 1–3 g of pyrite was used for samples with low Re contents (< 5 ppb). These samples were digested with HNO_3 in a 200 ml Carius tube employing a custom-made device based on the apparatus used by Qi et al. (2010). Any volatile Os released during digestion was trapped by 2 ml of 10 mol/l HCl in an ice–water bath. After the sulfides were
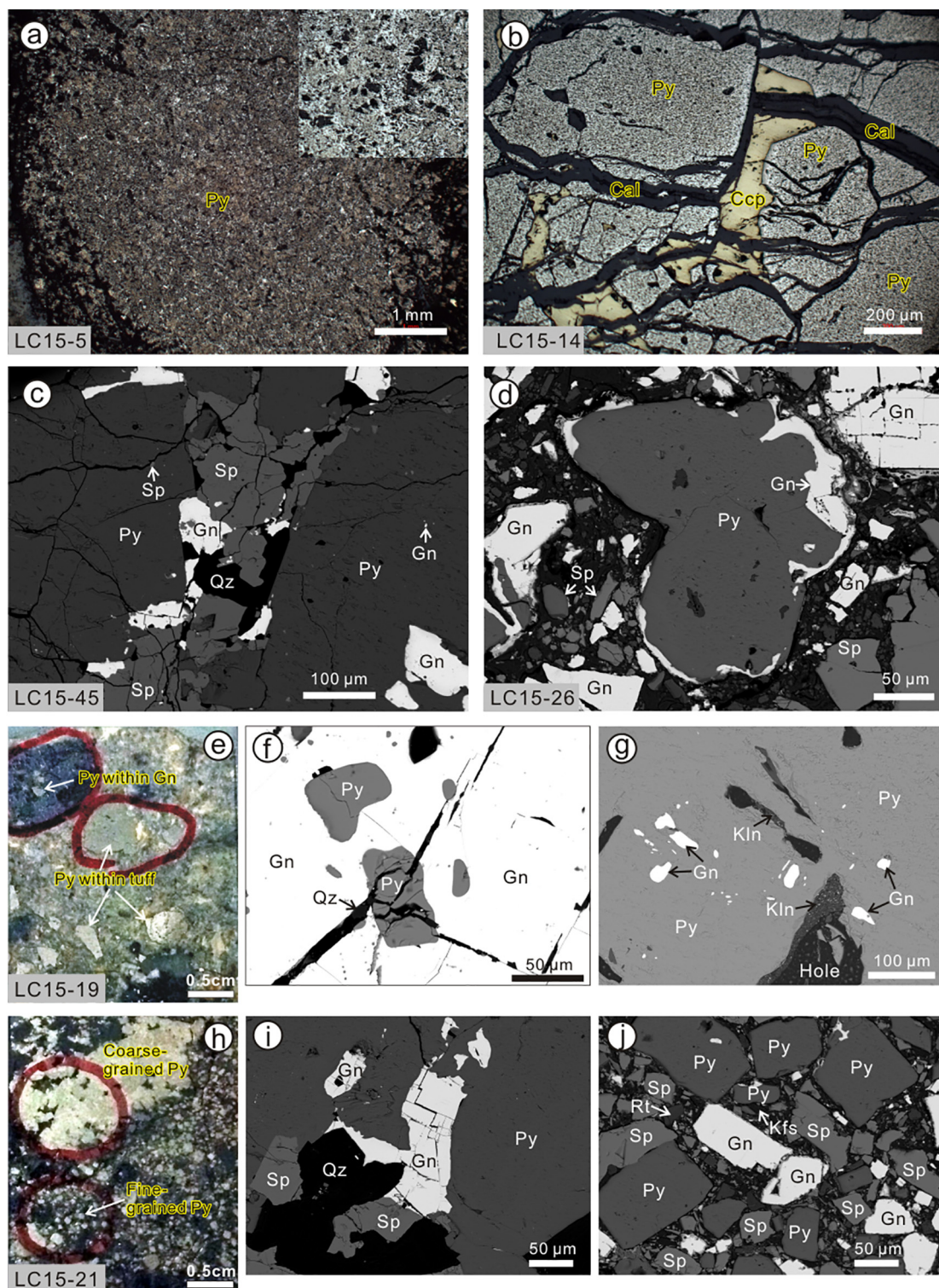
Fig. 4. Mineral observations of ores from the stratabound Pb–Zn–Ag mineralization. Fig. 4a–b shows reflected light images, whereas Fig. 4e and h are photomicrographs. Fig. 4c, d, f, g, i, and j are BSE images. (a) Fine-grained aggregates of pyrite forming a pyrite nodule (LC15-5). The inset at upper right is a 5× enlargement of part of the image. (b) Subhedral to euhedral pyrite and associated chalcopyrite cut by later calcite veins (LC15-14). (c) Subhedral pyrite associated with subhedral sphalerite and galena (LC15-45). Quartz formed later than pyrite, sphalerite, and galena. (d) Subhedral pyrite coexisting with but not in equilibrium with subhedral sphalerite and anhedral to subhedral galena (LC15-26). Pyrite is commonly replaced by galena. (e) Photomicrograph (LC15-19) showing two occurrences of pyrite (i.e., pyrite within galena (f) and pyrite within tuff matrix (g)). (f) Subhedral pyrite in galena cut by quartz veins. (g) Minor galena and kaolinite enclosed in coarse-grained pyrite within a tuff matrix. (h) Photomicrograph (LC15-21) showing two occurrences of pyrite (i.e., coarse-grained pyrite (i) and fine-grained pyrite (j)). (i) Pyrite associated with galena, sphalerite, and quartz. (j) Subhedral to euhedral pyrite, sphalerite, and galena cemented by small sulfide grains and minor rutile and K-feldspar. Mineral abbreviations: *Py* = pyrite; *Ccp* = chalcopyrite; *Cal* = calcite; *Gn* = galena; *Sp* = sphalerite; *Qz* = quartz; *Kln* = kaolinite; *Rt* = rutile; *Kfs* = K-feldspar.
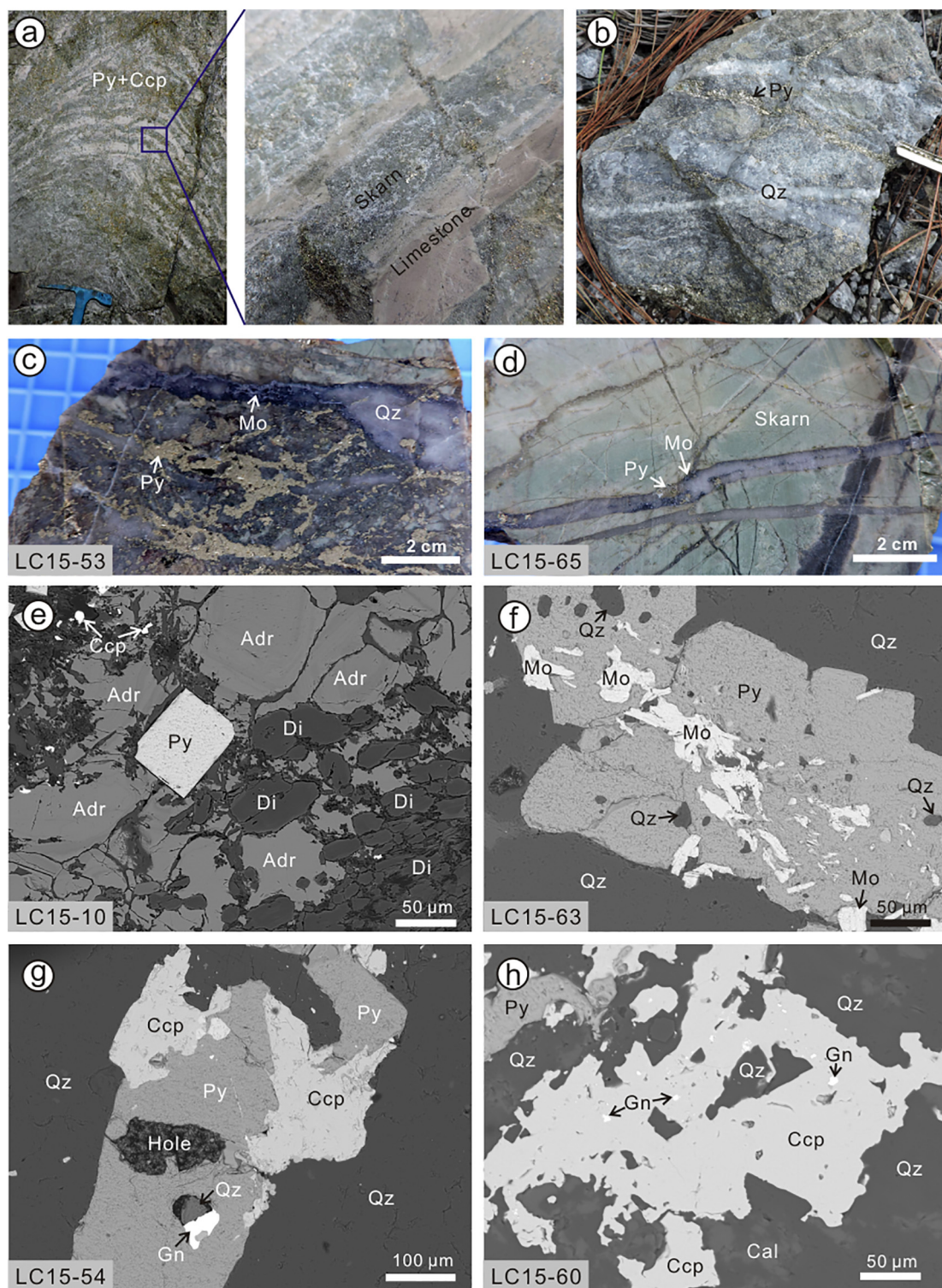
Fig. 5. Outcrop and ore photographs (a–d) and BSE images (e–h) of selected samples from the porphyry–skarn Mo mineralization in the Laochang deposit. (a) Interbedded skarn and limestone overprinted by massive sulfides (pyrite). The abrupt or transitional contact between skarn and limestone indicates that the skarn formed by hydrothermal replacement of limestone. (b) Stockwork ore composed mainly of pyrite and quartz. (c) Banded ore composed of pyrite, molybdenite, and quartz (LC15-53). Molybdenite–quartz vein crosscutting massive pyrite–quartz, indicating that molybdenite formed later than pyrite. (d) Skarn crosscut by pyrite–molybdenite–quartz veins, implying the later formation of sulfides (LC15-65). (e) Euhedral pyrite associated with andradite, diopside, and minor chalcopyrite (LC15-10). (f) Subhedral pyrite associated with molybdenite and quartz (LC15-63). (g) Pyrite associated with chalcopyrite and quartz (LC15-54). (h) Galena disseminated in chalcopyrite (LC15-60). Mineral abbreviations: *Py* = pyrite; *Ccp* = chalcopyrite; *Adr* = andradite; *Di* = diopside; *Cal* = calcite; *Gn* = galena; *Qz* = quartz; *Mo* = molybdenite.

Episode	Stratabound Pb-Zn-Ag mineralization		Porphyry-skarn Mo mineralization				
Stage	Early	Late	Skarn	Quartz	Early sulfide	Late sulfide	Carbonate
Colloidal pyrite							
Pyrite		★			★		
Chalcopyrite							
Galena							
Sphalerite							
Arsenopyrite							
Marcasite							
Pyrrhotite							
Argentite							
Native silver							
Lillianite							
Chiviatite							
Molybdenite							
Bismuthinite							
Stibnite							
Rabiagar							
Scheelite							
Cassiterite							
Diopside							
Garnet							
Vesuvianite							
Epidote							
Actinolite							
Chlorite							
Sericite							
Quartz							
Calcite							
Magnetite							
Siderite							
Fluorite							
Temperature (°C)	160-320		>400	200-350	230-340	220-300	190-280

★ Pyrite used for Re-Os, S isotopic and trace elemental analyses

Fig. 6. Paragenetic sequences of the stratabound Pb–Zn–Ag and porphyry–skarn Mo mineralization in the Laochang deposit (modified from Yang, 2014). Temperatures for each stage were inferred from the homogenization temperatures of fluid inclusions in quartz and calcite (Yang, 2014).

totally reacted with HNO_3, the HCl solution containing all the released Os was transferred back into the Carius tube. An appropriate amount of ^{185}Re-^{190}Os spike was added to the sample solution, and the resulting solution was further digested in aqua regia at 200 °C for ca. 10 h in a sealed Carius tube. Osmium was separated from the solution as OsO_4 using in situ distillation equipment, and Re was separated from the remaining solution after Os distillation using anion exchange resin (Biorad AG 1 × 8, 200–400 mesh) (Qi et al., 2007, 2010). An iridium standard solution (^{193}Ir/^{191}Ir = 1.6810) was added to the Re- and Os-bearing solutions for mass discrimination correction (Schoenberg et al., 2000; Huang et al., 2013b). Procedural blanks were 7.0 ± 1.0 pg (n = 2) and 1.5 ± 0.1 pg (n = 2) for Re and Os, respectively, with an average ^{187}Os/^{188}Os blank value of 0.55 ± 0.10 (1σ; n = 2). Absolute uncertainties (2σ) were derived from error propagation of uncertainties in Re and Os mass spectrometry measurements, blank abundances and isotopic compositions, and spike calibrations.

4.2. Sulfur isotope analysis

Sulfur isotopes were analyzed with an elemental analyzer–isotope ratio mass spectrometer (EA–IRMS), using a Thermo Scientific Flash 2000 high-temperature elemental analyzer coupled to a Thermo Scientific MAT 253 mass spectrometer at the SKLODG, IGCAS. The method used in this study was similar to that described by Huang et al. (2015). Appropriate amounts (~106–118 μg) of powdered pyrite separates were weighed and packed in tinfoil. Sulfur in pyrite was converted to SO_2 for isotopic analysis by burning in the reactor at a constant temperature of ca. 1000 °C using a stream of purified oxygen. The SO_2 was then carried by helium into the mass spectrometer. The sulfur isotopic compositions are reported using δ-notation in per mil (‰) relative to Vienna-Canyon Diablo Troilite (VCDT). Replicate analyses of Chinese Ag_2S standard GBW04415 yielded $δ^{34}S$ values of 22.13 ± 0.08‰ (1σ; n = 12), which is in good agreement with the

certified value of 22.15 ± 0.14‰ (1σ) (Ding et al., 2001).

4.3. In situ LA–ICP–MS trace element analysis

Trace element contents of pyrite were determined with an Agilent 7700× quadrupole ICP–MS coupled to a Photon Machines Excite 193 nm excimer laser ablation system at Nanjing FocuMs Technology, Nanjing, China. The authors selected ablation spots on thin sections and performed data processing. The analytical method is similar to that described by Gao et al. (2015) and Zhang et al. (2016), apart from the equipment types and analytical conditions for the laser ablation system and mass spectrometer. In our method, quantitative analysis was performed without prior knowledge and input of internal standard element concentrations for each ablation spot. To enhance the sensitivity and lower the instrument background, two pumps (rotary vane and turbo-molecular pumps) were used for the vacuum system. The laser was operated with 40 μm diameter ablation spots, at a repetition rate of 8 Hz and an energy of ~5 mJ per pulse. Each analysis comprised 40 s of ablation and data acquisition after measuring the gas blank for 15 s. Off-line signal selection, integration, time-drift correction, and quantitative calibration were performed by ICPMSDataCal (Liu et al., 2008). Sample signal intensities were converted to elemental concentrations via external calibration against USGS GSE-1G (synthetic basaltic glass) and GSC 12744 (pyrite) standards. Results were then normalized to 100% total element abundance (Halicz and Günther, 2004). The precision of each analysis is better than 20% for most elements that occur at concentrations of > 1 ppm, and up to 25% for those elements that occur at concentrations of < 1 ppm.

5. Results

5.1. Re-Os isotopic systematics

Pyrite from the stratabound Pb–Zn–Ag ores contains 0.4–16.6 ppb Re and 15.5–57.9 ppt Os (Table 1). The $^{187}Re/^{188}Os$ ratios range from 135 to 2688, and $^{187}Os/^{188}Os$ ratios vary from 0.9 to 7.5. The correlation coefficients (rho) between $^{187}Re/^{188}Os$ and $^{187}Os/^{188}Os$ ratios range from 0.29 to 0.86 (Table 1). Re-Os isotopic data for six pyrite separates yield a statistically meaningless isochron age of 68 ± 200 Ma with a mean square weighted deviation (MSWD) of 30 (Fig. 7a). As

shown in Fig. 7b, samples from the stratabound Pb–Zn–Ag mineralization can be broadly divided into two groups according to linear trends in Re-Os isotopic compositions. One group (samples LC15-50 and LC15-26) falls close to a 308 Ma sphalerite and galena Re-Os isochron for the stratabound Pb–Zn–Ag mineralization (Liu et al., 2015). The other group (samples LC15-45, LC15-23, and LC15-42) falls near the 47 Ma pyrite Re-Os isochron for the porphyry-skarn mineralization (Fig. 7b). Pyrite separates from the porphyry–skarn Mo ores contain 2.0–45.5 ppb Re and 12.8–37.4 ppt Os (Table 1). These pyrite separates have $^{187}Re/^{188}Os$ and $^{187}Os/^{188}Os$ ratios of 771 to 18,570 and 1.85 to 15.7, respectively. The correlation coefficients between these ratios range from 0.36 to 0.91. Analyses of six pyrite grains from the porphyry–skarn mineralization yielded an isochron age of 47.3 ± 4.8 Ma with an initial $^{187}Os/^{188}Os$ ratio of 1.13 ± 0.33 (2 σ; MSWD = 4.0; Fig. 7c).

5.2. Sulfur isotope systematics

Sulfur isotope data for sulfides from the Laochang deposit are compiled in Table 2 and illustrated in Fig. 8. Pyrite from the stratabound Pb–Zn–Ag mineralization yields $\delta^{34}S$ values of −2.1‰ to 1.9‰, and galena has similar $\delta^{34}S$ values of −1.7‰ to 2.4‰. Sphalerite and chalcopyrite from the stratabound Pb–Zn–Ag mineralization yield similar $\delta^{34}S$ values of −0.5‰ to 1.2‰. Realgar from the stratabound Pb–Zn–Ag mineralization has $\delta^{34}S$ values of 2.1‰ to 2.8‰.

Pyrite from the porphyry–skarn Mo mineralization has $\delta^{34}S$ values of −1.1‰ to 2.6‰. Sphalerite and galena from the porphyry–skarn Mo mineralization yield similar $\delta^{34}S$ values of −3.3‰ to −1.1‰. Molybdenite from the porphyry–skarn mineralization has $\delta^{34}S$ values from −4.0‰ to 0.3‰.

In general, sulfides from the stratabound Pb–Zn–Ag mineralization have $\delta^{34}S$ values of −2.1‰ to 2.8‰, with an average of 0.4‰, whereas those from the porphyry–skarn Mo mineralization have $\delta^{34}S$ values of −4.0‰ to 2.6‰ with an average of 0.5‰.

5.3. Trace element data

Average trace element data for the pyrite samples are listed in Table 3 and full analytical data are listed in Appendix B. Pyrite from the Laochang deposit contains a broad suite of measurable trace elements

Table 1
Re-Os data of pyrite from the Laochang deposit.

Sample no.	Sample wt.	Associated minerals[a]	Total Re (ppb)	2σ[b]	Total Os (ppb)	2σ	Common Os (ppb)	2σ	$^{187}Re/^{188}Os$	2σ	$^{187}Os/^{188}Os$	2σ	rho[c]	^{187}Os/Total Os (%)[d]
Stratabound Pb-Zn-Ag														
LC15-23	1.0002	Gn	11.9	0.41	0.0579	0.0199	0.0532	0.0165	1012	316	1.53	0.48	0.88	17
LC15-26	0.9983	Gn, Sp	5.8	0.23	0.0494	0.0211	0.0272	0.0045	971	165	7.50	1.30	0.86	55
LC15-42	0.5057	Gn, Ccp	16.6	0.34	0.0398	0.0228	0.0280	0.0065	2688	625	4.40	1.00	0.79	41
LC15-45	2.9984	Sp, Gn	2.4	0.16	0.0186	0.0057	0.0172	0.0040	629	154	1.45	0.35	0.64	16
LC15-50	3.0067	Gn, Ccp	0.4	0.04	0.0155	0.0073	0.0130	0.0050	135	55	2.37	0.92	0.73	24
LC15-51	2.9975	Gn, Ccp	0.5	0.03	0.0165	0.0037	0.0163	0.0023	135	21	0.90	0.13	0.29	11
Porphyry-skarn Mo														
LC15-53	0.5015	Mo, Ccp, Qz	42.2	0.91	0.0374	0.0051	0.0162	0.0020	10,840	1377	10.8	1.39	0.88	59
LC15-54	0.5028	Ccp, Gn, Qz	45.5	0.33	0.0298	0.0030	0.0102	0.0009	18,570	1732	15.7	1.51	0.91	68
LC15-63	0.5009	Mo, Ccp, Qz, Adr	8.6	0.41	0.0246	0.0045	0.0197	0.0025	1820	243	2.44	0.31	0.44	24
LC15-64	0.5008	Mo, Ccp, Qz, Adr, Di	13.2	0.55	0.0176	0.0022	0.0112	0.0014	4883	624	4.98	0.61	0.90	40
LC15-65	0.5005	Mo, Qz	28.1	1.01	0.0366	0.0015	0.0233	0.0007	5024	230	4.98	0.18	0.36	40
LC15-68	0.5015	Ab, Kfs, Qz, Chl	2.0	0.08	0.0128	0.0013	0.0109	0.0005	771	47	1.85	0.10	−0.39	20

[a] Minerals associated with pyrite listed as decreasing amounts. Mineral abbreviations: *Gn* = galena; *Sp* = sphalerite; *Ccp* = chalcopyrite; *Mo* = molybdenite; *Qz* = quartz; *Adr* = andradite; *Di* = diopside; *Ab* = albite; *Kfs* = K-feldspar; *Chl* = chlorite.
[b] Uncertainties reported at the 2 sigma level. All uncertainties are determined by error propagation of uncertainties in Re and Os mass spectrometer measurements, blank abundances and isotopic compositions, and spike calibrations.
[c] rho means uncertainty correlation factor, which is applied to assess the degree of correlation between $^{187}Re/^{188}Os$ and $^{187}Os/^{188}Os$ ratios (Ludwig, 1980).
[d] The proportion of ^{187}Os contents in total Os contents.
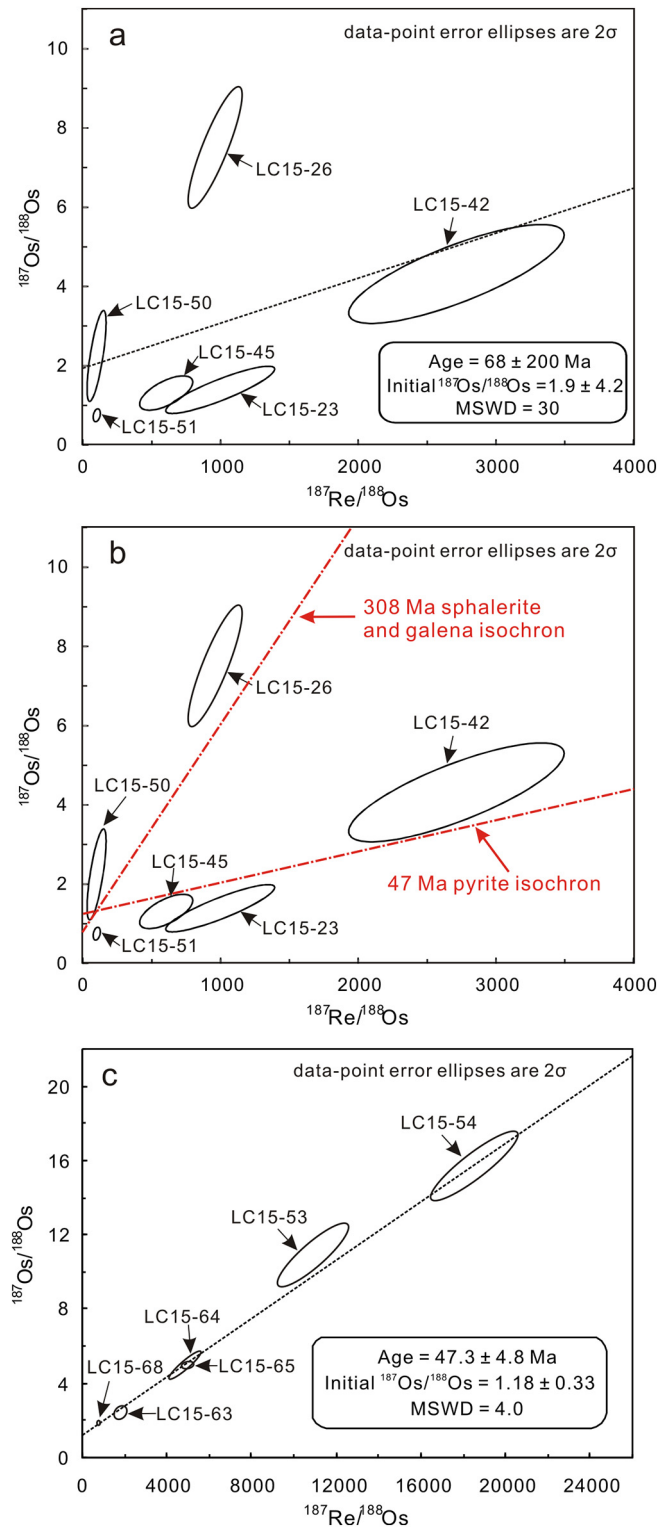
**Fig. 7.** ^{187}Re/^{188}Os vs. ^{187}Os/^{188}Os plots for pyrite separates from the strata-bound Pb–Zn–Ag and porphyry–skarn ores of the Laochang deposit. (a) Pyrite separates from the stratabound Pb–Zn–Ag mineralization failed to yield a geologically or statistically meaningful isochron age. (b) Comparison of Re-Os isotopic data of pyrite from the stratabound Pb–Zn–Ag mineralization with the 308 Ma sphalerite and galena Re-Os isochron line (Liu et al., 2015) and 47 Ma pyrite Re-Os isochron line (this study). (c) Regression of pyrite Re-Os data for the porphyry–skarn Mo mineralization. Isoplot/Ex 4.15 version was used to create a linear regression of Re-Os isotope data and correlation coefficients (rho; Table 1). *MSWD* = mean square weighted deviation.

including Ti, V, Cr, Mn, Co, Ni, Cu, Zn, As, Se, Te, Mo, Sb, Cd, and Pb. The trace element contents differ between the pyrite generations (Fig. 4e–j and 9a–b) and mineralization types (Fig. 9c). For sample LC15-19, pyrite within silicate (early pyrite; Fig. 4f) has higher Zn and Sb contents, but lower As, Te, and Pb contents than pyrite within galena (late pyrite; Fig. 4g) (Fig. 9a). For sample LC15-21, coarse-grained pyrite (early pyrite; Fig. 4i) has higher Co, Ni, Cu, As, Ag, Cd, and Sn contents, but lower V, Mn, Ga, Te, and Pb contents than fine-grained pyrite (late pyrite; Fig. 4j) (Fig. 9b). In general, pyrite from the stratabound Pb–Zn–Ag ores has higher V, Mn, Cu, Zn, Ga, As, Mo, Ag, Cd, Sn, Sb, Pb, and Bi contents, and lower Co, Ni, and Se contents than pyrite from the porphyry–skarn ores (Fig. 9c). Pyrite from both types of ore has similar average contents of Ti, Cr, Ge, and Te. Pyrite from the stratabound Pb–Zn–Ag mineralization has Se contents of 0.5–52 ppm (average = 9 ppm) and Se/S molar ratios of 0.3–40 × 10^{-6} (average = 7.6 × 10^{-6}), whereas pyrite from the porphyry-skarn Mo mineralization has Se contents of 1.6–78 ppm (average = 31 ppm) and Se/S ratios of 1–59 × 10^{-6} (average = 25 × 10^{-6}) (Appendix B).

Pyrite from the two types of mineralization has variable Co and Ni contents (Appendix B; Fig. 10a), and that from the stratabound Pb–Zn–Ag mineralization yields 0.02–8731 ppm Co, 0.08–515 ppm Ni, and Co/Ni ratios of 0.01–167, whereas pyrite from the porphyry-skarn Mo mineralization yields 0.07–8971 ppm Co, 3.3–1719 ppm Ni, and Co/Ni ratios of 0.01–259 (Appendix B; Fig. 10a). In diagrams of Co vs. Ni and As vs. other elements, pyrite grains from the stratabound Pb–Zn–Ag and porphyry–skarn Mo mineralization define two distinct populations (Fig. 10).

6. Discussion

6.1. Ages of the stratabound Pb–Zn–Ag and porphyry–skarn mineralization

Several methods have been used to constrain the age of the strata-bound Pb–Zn–Ag mineralization and underlying porphyry–skarn Mo mineralization in the Laochang deposit (Fig. 11). Wang et al. (1997) reported two groups of Pb-Pb model ages for sulfide ores (357–217 and 116–44 Ma), which were considered to represent the approximate ages of stratabound Pb–Zn–Ag and porphyry–skarn Mo mineralization. Sphalerite and galena data of the stratabound Pb–Zn–Ag ores of the Laochang deposit yield a Re-Os isochron age of 308 ± 25 Ma (Liu et al., 2015). In spite of a large uncertainty (~8%) of the sphalerite and galena Re-Os age, we believe that the Re-Os age is reliable, because: 1) the Re-Os isotope analytical method for galena and sphalerite has been improved by optimizing the chemical procedure; 2) the analyzed galena and sphalerite in Liu et al. (2015) have relatively high Re (~2–40 ppb) and Os (~25 to 270 ppt) contents that can be precisely analyzed by ICP-MS; and 3) the MSWD from the sphalerite-galena Re-Os isochron is close to 1, which reflects the appropriate error estimation (Ludwig, 2003). The sphalerite-galena Re-Os age is in agreement with the zircon U-Pb age (316–324 Ma) of the host volcanic rocks (Chen et al., 2010; Liang, 2014; X.-D. Deng et al., 2016) and is thus considered to represent the timing of the stratabound Pb–Zn–Ag mineralization. The Re-Os age above is different from the Rb-Sr isochron age of 45 ± 4 Ma for sphalerite from the stratabound Pb–Zn–Ag ores (Long et al., 2008). Due to unknown sample detail, the sphalerite Rb-Sr age cannot be eval-uated. X.-D. Deng et al. (2016) reported a pyrite Re-Os isochron age of 45.7 ± 3.1 Ma and a U-Pb age of 43.4 ± 1.2 Ma for titanite from the Pb–Zn–Ag ores. These isotopic ages are consistent with the ages (44–50 Ma) of the granite porphyry (Xu and Ouyang, 1991; Li et al., 2010a) and related Mo mineralization (Li et al., 2009a). This led X.-D. Deng et al. (2016) to propose that the stratabound Pb–Zn–Ag miner-alization and underlying porphyry–skarn Mo mineralization are the products of a common magmatic–hydrothermal fluid, and they argued against a VMS origin for the Pb–Zn–Ag mineralization (X.-D. Deng et al., 2016).

Pyrite separates from the porphyry–skarn Mo mineralization have a

Table 2
Sulfur isotope composition of sulfides from the Laochang deposit, SW China.

Sample no.	Sample location	Mineralization type[a]	Mineral[b]	$\delta^{34}S$ (‰)	$\delta^{34}S_{H2S}$ (‰)[c]	References	Sample no.	Sample location	Mineralization type	Mineral	$\delta^{34}S$ (‰)	$\delta^{34}S_{H2S}$ (‰)	References
LC15-20	1700 m mining adit, No. I orebody	Stratabound	Py	1.6	0.4	This study	LC09L10-2	No. I orebody	Stratabound	Py	0.7	−0.5	Liang (2014)
LC15-21	1895 m mining adit, No. IV orebody	Stratabound	Py	1.4	0.2	This study	LC09L10-4	No. I orebody	Stratabound	Py	0.9	−0.3	Liang (2014)
LC15-23	1895 m mining adit, No. IV orebody	Stratabound	Py	1.4	0.2	This study	LC09L10-9	No. I orebody	Stratabound	Py	1	−0.2	Liang (2014)
LC15-24	1895 m mining adit, No. IV orebody	Stratabound	Py	1.2	0.0	This study	LC09L15-3C	No. II orebody	Stratabound	Py	1.1	−0.1	Liang (2014)
LC15-26	1895 m mining adit, No. IV orebody	Stratabound	Py	1.6	0.4	This study	LC09L15-4C	No. II orebody	Stratabound	Py	0.9	−0.3	Liang (2014)
LC15-30	1650 m mining adit, No. II orebody	Stratabound	Py	1.9	0.7	This study	LC09L10-11	No. I orebody	Stratabound	Py	0	−1.2	Liang (2014)
LC15-42	1640 m mining adit, No. II orebody	Stratabound	Py	1.0	−0.2	This study	LC09L10-12	No. I orebody	Stratabound	Py	−0.3	−1.5	Liang (2014)
LC15-45	1640 m mining adit, No. I orebody	Stratabound	Py	1.2	0.0	This study	LC09L10-13	No. I orebody	Stratabound	Py	1	−0.2	Liang (2014)
LC15-50	1640 m mining adit, No. I orebody	Stratabound	Py	1.3	0.1	This study	LC09L11-1	No. I orebody	Stratabound	Py	1.5	0.3	Liang (2014)
LC15-51	1640 m mining adit, No. I orebody	Stratabound	Py	1.9	0.7	This study	LC09L11-3	No. I orebody	Stratabound	Py	1.1	−0.1	Liang (2014)
LC15-52	1650 m mining adit, No. I orebody	Stratabound	Py	1.5	0.3	This study	LC09L12-1	No. I orebody	Stratabound	Py	0.2	−1.0	Liang (2014)
LC15-53	1480 m mining adit	Porphyry-skarn	Py	2.2	1.2	This study	LC09L12-2	No. I orebody	Stratabound	Sp	−0.3	−1.5	Liang (2014)
LC15-54	1480 m mining adit	Porphyry-skarn	Py	2.0	1.0	This study	LC09L09-2A	No. I orebody	Stratabound	Sp	−0.3	−0.6	Liang (2014)
LC15-56	1480 m mining adit	Porphyry-skarn	Py	2.6	1.6	This study	LC09L13-6-S	No. I orebody	Stratabound	Sp	−0.4	−0.7	Liang (2014)
LC15-58	1480 m mining adit	Porphyry-skarn	Py	2.3	1.3	This study	LC09L15-1A	No. II orebody	Stratabound	Sp	1.2	0.9	Liang (2014)
LC15-60	1480 m mining adit	Porphyry-skarn	Py	1.9	0.9	This study	LC09L15-2-S	No. II orebody	Stratabound	Sp	0.2	−0.1	Liang (2014)
LC15-63	1480 m mining adit	Porphyry-skarn	Py	1.9	0.9	This study	LC09L15-3A	No. II orebody	Stratabound	Sp	0.7	0.4	Liang (2014)
LC15-64	1480 m mining adit	Porphyry-skarn	Py	2.3	1.3	This study	LC09L15-4A	No. II orebody	Stratabound	Sp	0.4	0.1	Liang (2014)
LC15-65	1480 m mining adit	Porphyry-skarn	Py	2.3	1.3	This study	LC09L15-12A	No. II orebody	Stratabound	Sp	1.2	0.9	Liang (2014)
LC15-66	1480 m mining adit	Porphyry-skarn	Py	2.0	1.0	This study	LC09L09-2B	No. I orebody	Stratabound	Gn	−1.4	0.5	Liang (2014)
LC15-68	1480 m mining adit	Porphyry-skarn	Py	2.3	1.3	This study	LC09L10-4G	No. I orebody	Stratabound	Gn	−1.2	0.7	Liang (2014)
1600-B1	1600 m mining adit	Porphyry-skarn	Py	1.8	0.8	This study	LC09L13-2G	No. II orebody	Stratabound	Gn	−0.2	1.7	Liang (2014)
1600-B3-1	1600 m mining adit	Porphyry-skarn	Py	−1.1	−2.1	Zhao et al. (2012)	LC09L15-1B	No. II orebody	Stratabound	Gn	−0.6	1.3	Li et al. (2015)
1600-B3-3	1600 m mining adit	Porphyry-skarn	Gn	−2.4	−0.8	Zhao et al. (2012)	LC09L15-2G	No. II orebody	Stratabound	Gn	−0.7	1.2	Li et al. (2015)
1600-B3-2	1600 m mining adit	Porphyry-skarn	Sp	−3.3	−3.6	Zhao et al. (2012)	LC09L15-3B	No. II orebody	Stratabound	Gn	−0.8	1.1	Li et al. (2015)
ZK14703-1	Drill hole ZK14703	Porphyry-skarn	Sp	−1.1	−1.4	Zhao et al. (2012)	LC09L15-4B	No. II orebody	Stratabound	Gn	−1.1	0.8	Li et al. (2015)
TW-4	Drill hole ZK14827	Porphyry-skarn	Mo	−1.0	−2.2	Zhao et al. (2012)	LC09L15-14C	No. II orebody	Stratabound	Ccp	0	−0.2	Li et al. (2015)
TW-5	Drill hole ZK14827	Porphyry-skarn	Mo	−1.1	−2.3	Zhao et al. (2012)	LC09L15-16C	No. II orebody	Stratabound	Ccp	−0.5	−0.7	Li et al. (2015)
TW-6	Drill hole ZK14827	Porphyry-skarn	Mo	−4.0	−5.2	Zhao et al. (2012)	LC02-2	No. I orebody	Stratabound	Py	−0.7	−1.9	Li et al. (2015)
TW-7	Drill hole ZK14827	Porphyry-skarn	Mo	0.3	−0.9	Zhao et al. (2012)	LC02-3	No. I orebody	Stratabound	Py	−2.1	−3.3	Li et al. (2015)
H13	Drill hole ZK152A04, No. I orebody	Stratabound	Py	1.8	0.6	Li et al. (1995)	LC06-1	No. I orebody	Stratabound	Py	0.1	−1.1	Li et al. (2015)
H14	Drill hole ZK152A03, No. II orebody	Stratabound	Py	1.8	0.6	Li et al. (1995)	LC09-1	No. I orebody	Stratabound	Py	0.5	−0.7	Li et al. (2015)
H15	Drill hole ZK152A03, No. II orebody	Stratabound	Py	1.8	0.6	Li et al. (1995)	LC09-2	No. I orebody	Stratabound	Sp	−0.3	−0.6	Li et al. (2015)
I1B	Drill hole ZK11-1, No. I orebody	Stratabound	Py	1.4	0.2	Li et al. (1995)	LC09-2	No. I orebody	Stratabound	Gn	−1.4	0.5	Li et al. (2015)
I2	Drill hole ZK11-1, No. I orebody	Stratabound	Py	1.3	0.1	Li et al. (1995)	LC09-3	No. I orebody	Stratabound	Py	0.1	−1.1	Li et al. (2015)
I6	95 old cave, mineralization veins	Stratabound	Py	1.5	0.3	Li et al. (1995)	LC10-1	No. I orebody	Stratabound	Py	−0.4	−1.6	Li et al. (2015)
I5B	Drill hole ZK1106, No. I orebody	Stratabound	Py	1.1	−0.1	Li et al. (1995)	LC10-2	No. I orebody	Stratabound	Py	0.7	−0.5	Li et al. (2015)
I6B	Drill hole ZK1901, No. I orebody	Stratabound	Py	1.1	−0.1	Li et al. (1995)	LC10-3	No. I orebody	Stratabound	Py	0.6	−0.6	Li et al. (2015)
I9	Drill hole ZK14904, No. II orebody	Stratabound	Py	1.3	0.1	Li et al. (1995)	LC10-4	No. I orebody	Stratabound	Py	0.9	−0.3	Li et al. (2015)
I14B	Drill hole ZK15004, No. II orebody	Stratabound	Py	1.6	0.4	Li et al. (1995)	LC10-9	No. I orebody	Stratabound	Gn	−1.2	0.7	Li et al. (2015)
I1A	Drill hole ZK11-1, No. I orebody	Stratabound	Gn	−1.3	0.6	Li et al. (1995)	LC10-11	No. I orebody	Stratabound	Py	1	−0.2	Li et al. (2015)
I5A	Drill hole ZK1106, No. I orebody	Stratabound	Gn	0.1	2.0	Li et al. (1995)	LC10-12	No. I orebody	Stratabound	Py	0	−1.2	Li et al. (2015)
I6A	Drill hole ZK1901, No. I orebody	Stratabound	Gn	0.8	2.7	Li et al. (1995)	LC10-13	No. I orebody	Stratabound	Py	−0.3	−1.5	Li et al. (2015)
I7	Drill hole ZK152A06, No. II orebody	Stratabound	Gn	0.4	2.3	Li et al. (1995)	LC11-1	No. I orebody	Stratabound	Py	1	−0.2	Li et al. (2015)
I10	Drill hole ZK15004, mineralization veins	Stratabound	Gn	2.4	4.3	Li et al. (1995)	LC11-2	No. I orebody	Stratabound	Py	1.3	0.1	Li et al. (2015)
I14A	Drill hole ZK15004, No. II orebody	Stratabound	Gn	−0.1	1.8	Li et al. (1995)	LC11-3	No. I orebody	Stratabound	Py	1.1	−0.1	Li et al. (2015)
LC-1	1925 m mining adit, No. I orebody	Stratabound	Gn	−0.8	1.1	Li et al. (1995)	LC12-1	No. I orebody	Stratabound	Py	0.2	−1.0	Li et al. (2015)
LC-2	1925 m mining adit, No. I orebody	Stratabound	Sp	0.1	−0.2	Li et al. (1995)	LC13-2	No. I orebody	Stratabound	Gn	−0.2	−1.5	Li et al. (2015)
LC-3	1986 m mining adit, No. I orebody	Stratabound	Py	1.9	0.7	Li et al. (1995)	LC13-6	No. I orebody	Stratabound	Sp	−0.4	1.7	Li et al. (2015)
LC-4	1986 m mining adit, No. I orebody	Stratabound	Sp	0.4	0.1	Li et al. (1995)	LC15-1	No. II orebody	Stratabound	Sp	1.2	0.9	Li et al. (2015)
LC-5	1986 m mining adit, No. I orebody	Stratabound	Gn	−1.7	2.3	Li et al. (1995)							
LC-6	1975 m mining adit, No. I orebody	Stratabound	Gn	−0.6	0.2	Li et al. (1995)							

(continued on next page)

Table 2 (continued)

Sample no.	Sample location	Mineralization type[a]	Mineral[b]	δ34S (‰)	δ34S_H2S (‰)[c]	References
LC15-1	No. II orebody	Stratabound	Gn	-0.6	1.3	Li et al. (2015)
LC15-2	No. II orebody	Stratabound	Sp	0.2	-0.1	Li et al. (2015)
LC15-2	No. II orebody	Stratabound	Gn	-0.7	1.2	Li et al. (2015)
LC15-3	No. II orebody	Stratabound	Sp	0.7	0.4	Li et al. (2015)
LC15-3	No. II orebody	Stratabound	Gn	-0.8	1.1	Li et al. (2015)
LC15-3	No. II orebody	Stratabound	Py	1.1	-0.1	Li et al. (2015)
LC15-4	No. II orebody	Stratabound	Sp	0.4	0.1	Li et al. (2015)
LC15-4	No. II orebody	Stratabound	Gn	-1.1	0.8	Li et al. (2015)
LC15-4	No. II orebody	Stratabound	Py	0.9	-0.3	Li et al. (2015)
LC15-8	No. II orebody	Stratabound	Py	0.1	-1.1	Li et al. (2015)
LC15-12	No. II orebody	Stratabound	Sp	1.2	0.9	Li et al. (2015)
LC15-14	No. II orebody	Stratabound	Ccp	0	-0.2	Li et al. (2015)
LC15-16	No. II orebody	Stratabound	Ccp	-0.5	-0.7	Li et al. (2015)
LC-7	1975 m mining adit, No. I orebody	Stratabound	Sp	0	-0.3	Li et al. (1995)
LC-8	Drill hole ZK14808, No. II orebody	Stratabound	Ccp	1.2	1.0	Li et al. (1995)
L1925-8	1925 m mining adit, No. I orebody	Stratabound	Rlg	2.6		Li et al. (1995)
L1925-9	1925 m mining adit, No. I orebody	Stratabound	Rlg	2.1		Li et al. (1995)
L1925-10	1925 m mining adit, No. I orebody	Stratabound	Rlg	2.8		Li et al. (1995)
LC09L02-2	No. I orebody	Stratabound	Py	-0.7	-1.9	Liang (2014)
LC09L0202	No. I orebody	Stratabound	Py	-2.1	-3.3	Liang (2014)
LC09L06-1	No. I orebody	Stratabound	Py	0.1	-1.1	Liang (2014)
LC09L11-2	No. I orebody	Stratabound	Py	1.3	0.1	Liang (2014)
LC09L15-8	No. II orebody	Stratabound	Py	0.1	-1.1	Liang (2014)
LC09L09-1	No. I orebody	Stratabound	Py	0.5	-0.7	Liang (2014)
LC09L09-1-j	No. I orebody	Stratabound	Py	0.1	-1.1	Liang (2014)
LC09L10-1	No. I orebody	Stratabound	Py	-0.4	-1.6	Liang (2014)
LC09L10-1-j	No. I orebody	Stratabound	Py	0.6	-0.6	Liang (2014)

[a] Stratabound = stratabound Pb-Zn-Ag mineralization; Porphyry-skarn = porphyry-skarn Mo mineralization.

[b] Mineral abbreviations: Py = pyrite; Sp = sphalerite; Gn = galena; Ccp = chalcopyrite; Rlg = realgar; Mo = molybdenite.

[c] δ34S values of H$_2$S in fluid in equilibrium with the sulfides. The calculation equation for pyrite, sphalerite, and molybdenite is from Ohmoto and Rye (1979), whereas that for chalcopyrite and galena is from Li and Liu (2006). Temperatures are 300 °C and 350 °C for the stratabound Pb-Zn-Ag and porphyry-skarn Mo mineralization (Yang, 2014).
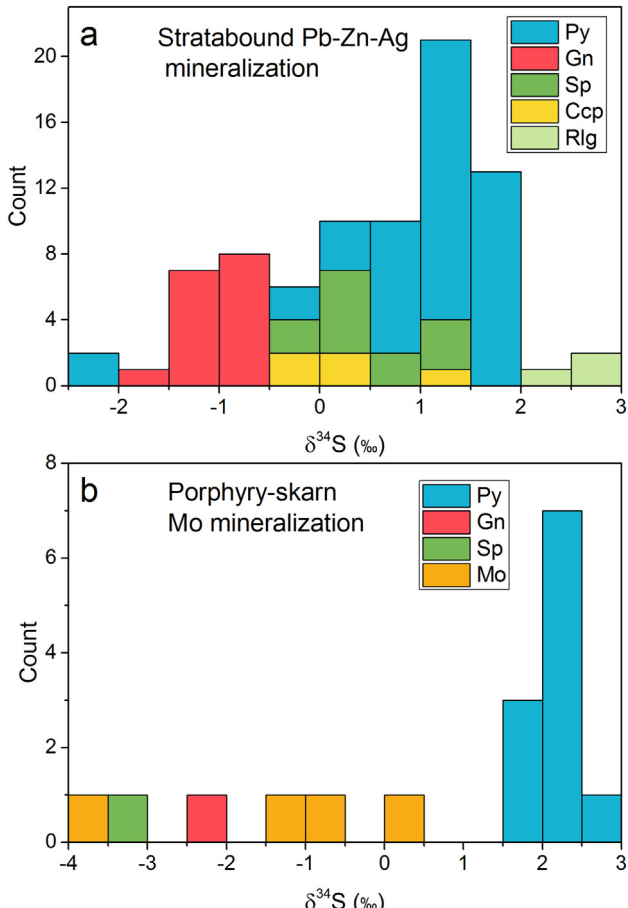
Fig. 8. Histogram of sulfur isotopic compositions of sulfides from the stratabound Pb–Zn–Ag (a) and porphyry–skarn Mo (b) mineralization in the Laochang deposit. Mineral abbreviations: *Py* = pyrite; *Ccp* = chalcopyrite; *Gn* = galena; *Sp* = sphalerite; *Mo* = molybdenite; *Rlg* = realgar. Data sources: Li et al. (1995, 2015); Zhao et al. (2012); Liang (2014); this study.

Re-Os isochron age of 47.3 ± 4.8 Ma (Fig. 7c), consistent with a previous molybdenite Re-Os age (44.2 ± 0.3 Ma; Li et al., 2009a) for quartz–sulfide ores and zircon U-Pb ages (~45–50 Ma; Li et al., 2010a; Xu and Ouyang, 1991) for the granite porphyry (Fig. 11). Our Re-Os dating of pyrite from the Pb–Zn–Ag ores did not yield a meaningful age (Fig. 7a). The open behavior of the pyrite Re-Os isotopic system in the Laochang deposit is similar to that in many sediment-hosted Pb-Zn deposits elsewhere (Spry et al., 2014; Hnatyshin et al., 2016; Kelley et al., 2017), which may be due to multiple Os sources or post-ore remobilization.

As shown in Fig. 7b, data for pyrite samples from the stratabound Pb–Zn–Ag mineralization can be broadly divided into two groups. Data for one group are located near the 308 Ma regression line defined by sphalerite and galena (Liu et al., 2015), and data for the other group fall near the 47 Ma pyrite regression line for the porphyry–skarn Mo mineralization. This may indicate that the scatter in the data is due to different pyrite origins. However, the indistinguishable sulfur isotopic compositions of the two groups of samples imply similar sulfur sources. Moreover, trace element data for LC15-26 and LC15-45 (i.e., representing both groups) show no obvious differences in terms of Co, Ni, and Se contents (Table 3), indicating similar metal sources. Therefore, the scatter in the Re-Os isotopic data for the stratabound Pb–Zn–Ag mineralization cannot be explained by different pyrite origins, and is most likely due to post-ore remobilization. The Re-Os isotopic system can be perturbed by a variety of processes, such as hydrothermal or supergene alteration, deformation, and metamorphism (Lambert et al.,
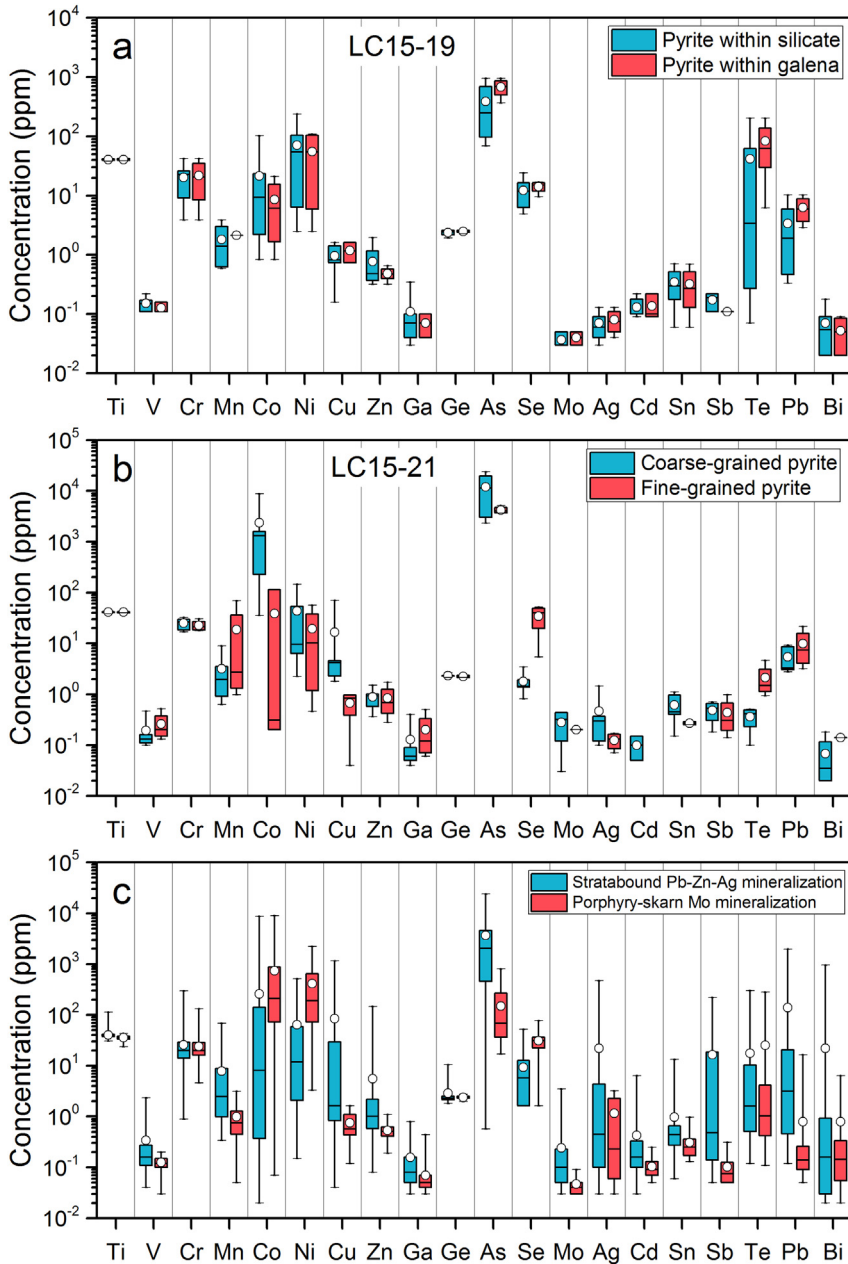
Fig. 9. Box and whisker plots showing the variations in trace element compositions of pyrite. (a) Comparison of the composition of pyrite within silicate and pyrite within galena (Fig. 4e–g). (b) Comparison of the composition of coarse- and fine-grained pyrite (Fig. 4h–j). (c) Comparison of the composition of stratabound Pb–Zn–Ag and porphyry–skarn Mo mineralization (based on all data). Whiskers represent the range of minimum and maximum values. The short line within each box represents the median value, which separates the box into two parts (i.e., lower 25–50 percentile group and upper 50–75 percentile). The white filled circle represents the average value.

1999; Ruiz and Mathur, 1999; Morelli et al., 2004; Tristá-Aguilera et al., 2006). Experimental studies have demonstrated that Re can be remobilized by oxidized hydrothermal fluids under high-temperature (> 400 °C) conditions (Xiong and Wood, 1999; Xiong et al., 2006). Therefore, we infer that the stratabound Pb–Zn–Ag ores were remobilized by post-ore, high-temperature hydrothermal fluids from the underlying porphyry system. We propose formation of stratabound Pb–Zn–Ag ores at 308 Ma (Li et al., 2015; Liu et al., 2015) and their partial remobilization at 47 Ma (Long et al., 2008; X.-D. Deng et al., 2016) due to their interaction with fluids associated with Eocene magmatism.

6.2. Isotopic constraints on the sources of the ore-forming fluids

Previous studies on the origins of the stratabound Pb–Zn–Ag and porphyry–skarn Mo mineralization have used C, H, O, S, and Pb isotope and fluid inclusion data (Ye et al., 1992; Li et al., 1995, 2015; Chen et al., 2011; Zhao et al., 2012; Liang, 2014; Yang, 2014). Pyrite,

sphalerite, chalcopyrite, and galena from the stratabound Pb–Zn–Ag mineralization have average $\delta^{34}S$ values of 0.7‰, 0.4‰, 0.04‰, and −0.6‰, respectively, whereas pyrite, sphalerite, and galena from the porphyry-skarn mineralization have average $\delta^{34}S$ values of 1.8‰, −2.2‰, and −2.4‰, respectively. In general, sulfides from the stratabound Pb–Zn–Ag and porphyry–skarn Mo mineralization have similar average $\delta^{34}S$ values (0.48‰ and 0.52‰, respectively; Table 2 and Fig. 9). The calculated average $\delta^{34}S$ values of H_2S in fluid in equilibrium with the sulfides are 0.03‰ and −0.3‰ for stratabound Pb–Zn–Ag and porphyry–skarn Mo mineralization, respectively (Table 2), indicating a magmatic origin for the sulfur. This result is consistent with previous studies (Li et al., 1995, 2015; Zhao et al., 2012; Liang, 2014; Yang, 2014). Sulfides (pyrite, galena, sphalerite, and chalcopyrite) from the stratabound Pb–Zn–Ag mineralization have $^{206}Pb/^{204}Pb$, $^{207}Pb/^{204}Pb$, and $^{208}Pb/^{204}Pb$ ratios of 18.486–18.684, 15.668–15.712, and 38.725–39.024, respectively (Ye et al., 1992; Li et al., 2015), which are indistinguishable from Pb isotope ratios of 17.860–18.700, 15.448–15.733, and 37.753–39.104 for sulfides from the

Table 3
The average trace element contents (in ppm) of pyrite from the stratabound Pb-Zn-Ag and porphyry-skarn Mo mineralization in the Laochang deposit.

Sample no.[a]		Ti	V	Cr	Mn	Co	Ni	Cu	Zn	Ga	Ge	As	Se	Mo	Ag	Cd	Sn	Sb	Te	Pb	Bi
Detection limit		0.887	0.070	1.171	0.185	0.018	0.073	0.074	0.118	0.021	0.383	0.932	0.045	0.015	0.018	0.041	0.11	0.043	0.15	0.024	0.010
Stratabound Pb-Zn-Ag																					
LC15-2	GM (n = 4)[b]	32.0	0.14	11.3	3.16	0.4	0.9	2.92	0.76	0.07	2.30	1209	7.14	0.03	0.03	0.06	0.26	0.08	48.2	0.24	0.13
	GSD[b]	1.0	2.28	1.6	3.11	19.9	1.9	3.09	1.20	3.39	1.04	2	2.11	2.67	4.39	2.16	1.69	1.98	8.0	30.02	35.71
LC15-5	GM (n = 4)	40.6	0.12	20.9	2.09	228	56.7	2.63	0.63	0.06	2.06	49	16.8	0.05	0.04	0.06	0.19	0.04	3.81	0.48	0.41
	GSD	1.1	1.22	2.1	2.73	5	2.2	6.98	2.46	2.46	1.09	10	1.3	8.32	3.52	2.31	2.89	1.39	7.19	3.46	30.41
LC15-6	GM (n = 4)	41.0	0.12	22.5	0.48	15.2	38.6	0.80	0.37	0.03	2.46	293	16.3	3.72	0.02	0.04	0.20	0.03	20.4	0.21	0.06
	GSD	1.0	1.49	1.4	2.48	35.5	19.1	1.18	1.53	3.06	1.10	3	1.4	2.46	1.52	2.31	2.08	1.00	2.5	1.42	12.34
LC15-16	GM (n = 6)	41.6	0.10	11.0	0.19	17.9	18.7	0.39	1.23	0.03	2.24	142	4.26	0.02	0.02	0.05	0.13	0.03	0.15	0.37	0.01
	GSD	1.1	1.46	2.3	2.58	4.7	4.2	3.11	1.31	1.96	1.09	3	1.43	2.49	2.99	2.60	1.94	1.00	1.75	1.92	1.54
LC15-19a	GM (n = 4)	40.6	0.10	15.6	0.26	4.5	22.4	1.09	0.47	0.03	2.49	637	13.8	0.02	0.07	0.09	0.25	0.04	46.6	5.58	0.04
	GSD	1.0	1.65	2.9	4.04	4.2	6.4	1.57	1.34	2.49	1.07	2	1.3	2.13	1.66	2.30	2.52	1.88	4.3	1.75	2.31
LC15-19b	GM (n = 4)	40.0	0.17	16.0	0.67	14.5	30.6	0.60	0.51	0.08	2.21	94	8.23	0.01	0.02	0.08	0.31	0.08	0.26	0.50	0.02
	GSD	1.0	1.22	2.1	4.00	5.4	7.0	2.46	4.07	2.81	1.14	1	2.08	1.65	1.52	2.16	1.89	2.98	2.05	1.54	4.67
LC15-21a	GM (n = 5)	41.2	0.16	24.0	2.04	682	16.0	5.58	0.79	0.08	2.34	8223	1.61	0.11	0.29	0.04	0.49	0.25	0.25	4.66	0.03
	GSD	1.1	1.87	1.3	2.89	8	5.4	4.33	1.74	2.50	1.08	3	1.70	5.32	2.92	2.04	2.23	3.64	2.21	1.81	3.37
LC15-21b	GM (n = 4)	41.1	0.23	22.0	4.52	0.6	5.5	0.41	0.68	0.14	2.24	4176	25.7	0.02	0.12	0.03	0.14	0.33	1.75	7.58	0.01
	GSD	1.0	1.82	1.3	6.65	45.8	8.8	4.71	2.12	2.57	1.06	1	2.9	4.26	1.52	1.00	2.05	2.27	1.99	2.31	4.47
LC15-26	GM (n = 7)	40.7	0.22	23.0	23.63	0.2	1.9	153	7.94	0.05	2.12	2237	0.91	0.04	4.51	0.15	1.14	48.68	0.12	418.58	0.01
	GSD	1.0	2.35	1.3	1.89	6.9	14.0	2	4.25	1.97	1.09	3	1.39	2.42	1.55	3.91	3.03	2.06	1.36	1.62	1.86
LC15-29	GM (n = 7)	41.7	0.11	19.1	0.65	0.0	0.2	2	0.26	0.02	2.18	3879	17.8	0.01	0.15	0.05	0.19	0.05	10.6	2.25	0.59
	GSD	1.1	1.77	2.3	4.06	0.0	7.1	1.17	6.09	2.74	1.09	1	1.4	1.63	11.07	2.28	2.32	1.95	3.1	9.02	17.27
LC15-31	GM (n = 3)	40.2	0.14	42.9	2.70	0.0	176	20.3	1.26	0.05	2.47	1498	0.28	0.06	0.27	0.05	0.37	0.45	2.14	6.38	0.03
	GSD	1.0	1.42	1.2	2.24	1.6	3	3.0	1.98	3.09	1.18	16	6.91	4.46	3.25	2.96	2.11	3.15	6.17	3.42	1.74
LC15-33	GM (n = 5)	34.8	0.16	17.8	1.67	4.9	2.9	0.91	0.96	0.06	2.20	1519	7.51	0.04	0.10	0.06	0.18	0.06	2.77	1.47	0.30
	GSD	1.1	1.57	1.4	3.31	5.8	6.1	2.22	3.22	2.27	1.11	4	2.91	6.32	3.98	2.04	2.26	2.24	9.16	3.85	21.76
LC15-34	GM (n = 5)	43.2	0.54	33.6	4.26	3.5	243	105	18.6	0.16	2.21	2158	0.16	0.06	5.03	0.53	4.04	6.24	0.31	192.52	0.07
	GSD	1.1	2.40	1.8	7.35	29.0	2	4	4.1	3.70	1.13	2	4.71	3.93	2.45	2.58	2.16	10.53	2.19	11.00	5.68
LC15-40	GM (n = 7)	35.7	0.14	8.1	1.10	11.6	3.6	2.60	1.28	0.02	2.49	6253	3.66	0.02	0.25	0.10	0.31	0.43	4.42	10.48	3.26
	GSD	1.1	2.52	2.7	3.79	19.7	6.4	6.37	1.38	1.30	1.09	2	4.29	2.44	25.33	3.40	2.54	18.57	2.80	18.09	25.11
LC15-44	GM (n = 5)	36.7	0.31	17.6	6.45	409	51.9	64.5	4.64	0.27	7.31	49	10.9	0.39	2.34	0.24	0.37	1.04	0.98	6.29	0.01
	GSD	1.1	5.97	1.4	1.72	1	1.1	18.7	2.53	3.32	1.46	34	1.1	3.57	2.04	3.94	2.09	5.21	1.37	5.00	1.00
LC15-45	GM (n = 9)	42.3	0.14	17.8	1.00	1.9	0.8	1.29	0.30	0.04	2.16	6998	0.78	0.03	0.02	0.06	0.31	0.07	0.29	0.71	0.01
	GSD	1.1	1.56	1.9	2.86	10.5	3.3	3.33	2.35	2.16	1.09	1	4.04	2.90	2.43	2.49	2.11	3.26	2.79	3.38	1.45
LC15-48	GM (n = 5)	38.1	1.43	58.6	14.65	392	50.6	317	4.42	0.29	7.56	711	7.24	0.31	200.33	0.98	0.66	21.48	0.97	228.58	0.03
	GSD	1.1	1.57	2.6	2.82	1	1.1	5	2.06	1.69	1.26	2	1.17	1.62	1.91	3.28	1.66	8.26	2.56	7.92	5.95
Porphyry-skarn Mo																					
LC15-10	GM (n = 5)	30.5	0.10	16.4	0.64	1293	1354	0.49	0.74	0.07	2.41	232	31.4	0.02	0.01	0.05	0.23	0.06	2.18	0.12	0.01
	GSD	1.2	1.47	2.2	1.82	2	2	1.82	1.31	3.54	1.04	1	1.1	2.29	1.00	1.85	1.18	1.95	2.32	2.28	1.00
LC15-53	GM (n = 5)	37.3	0.12	25.6	0.23	29.1	9.1	0.50	0.50	0.05	2.37	186	13.4	0.03	0.01	0.04	0.42	0.03	0.11	0.08	0.01
	GSD	1.0	1.40	1.5	3.49	31.0	1.8	1.92	1.54	2.63	1.11	2	3.4	2.21	1.00	1.35	2.86	1.24	1.10	1.35	2.41
LC15-54	GM (n = 5)	37.1	0.10	21.6	0.80	168	679	1.05	0.60	0.03	2.37	49	34.9	0.01	0.04	0.05	0.31	0.04	0.23	0.74	0.02
	GSD	1.1	2.08	1.4	1.97	4	2	1.39	1.20	1.72	1.12	2	1.4	1.57	9.42	1.75	2.23	1.57	3.01	5.76	10.09
LC15-56	GM (n = 5)	36.3	0.12	17.0	1.04	148	187	0.48	0.38	0.05	2.32	49	16.2	0.02	0.04	0.08	0.18	0.06	0.59	0.31	0.05
	GSD	1.1	1.70	2.3	3.61	9	3	2.52	2.49	2.12	1.11	1	3.0	1.73	11.76	2.70	2.46	1.75	6.10	7.27	21.09
LC15-58	GM (n = 5)	38.2	0.15	32.5	1.07	240	48.4	0.70	0.55	0.05	2.41	43	27.8	0.01	0.01	0.06	0.18	0.07	0.25	0.39	0.03
	GSD	1.0	1.16	2.3	2.08	6	2.0	1.79	1.52	2.05	1.03	2	1.3	1.00	1.00	2.14	1.66	3.13	2.07	2.08	3.24
LC15-60	GM (n = 3)	32.5	0.12	14.8	0.30	73.0	199	0.43	0.26	0.02	2.41	67	15.1	0.01	0.01	0.05	0.18	0.04	1.65	0.06	0.08
	GSD	1.0	1.14	1.1	2.26	1.4	3	6.32	2.69	1.49	1.04	3	2.0	1.00	1.00	2.16	2.35	1.32	15.22	3.04	7.96
LC15-63	GM (n = 5)	34.4	0.11	17.3	0.70	84.2	617	0.50	0.42	0.03	2.33	293	41.4	0.01	0.01	0.09	0.18	0.07	0.81	0.15	0.03
	GSD	1.0	1.26	1.3	2.81	2.1	2	2.10	1.41	1.93	1.07	1	1.4	1.00	1.00	1.42	1.82	2.02	3.30	1.21	7.77
LC15-66	GM (n = 4)	38.5	0.10	21.3	0.35	57.0	147	0.49	0.33	0.03	2.41	37	19.0	0.02	0.01	0.08	0.15	0.05	0.25	0.14	0.01
	GSD	1.1	1.69	1.4	3.70	4.3	2	1.93	1.77	2.23	1.04	2	1.5	2.86	1.00	2.22	1.71	2.48	1.97	1.75	2.10

(continued on next page)

Table 3 (*continued*)

Sample no.[a]		Ti	V	Cr	Mn	Co	Ni	Cu	Zn	Ga	Ge	As	Se	Mo	Ag	Cd	Sn	Sb	Te	Pb	Bi
Detection limit		0.887	0.070	1.171	0.185	0.018	0.073	0.074	0.118	0.021	0.383	0.932	0.045	0.015	0.018	0.041	0.11	0.043	0.15	0.024	0.010
LC15-67	GM (n = 5)	34.2	0.11	20.4	0.39	766	258	1.09	0.45	0.04	2.31	327	51.7	0.01	0.02	0.07	0.17	0.04	128	0.19	0.04
	GSD	1.0	1.29	1.5	2.46	3	2	1.15	1.34	1.78	1.07	2	1.4	1.57	1.98	1.75	1.80	1.34	2	2.49	14.91
LC15-68	GM (n = 5)	36.1	0.12	20.4	0.51	757	74.7	0.25	0.45	0.04	2.39	26	30.3	0.01	0.02	0.08	0.15	0.04	0.18	0.07	0.01
	GSD	1.0	1.13	1.6	2.30	3	1.4	2.67	1.24	1.82	1.09	1	1.2	1.00	3.61	2.11	1.55	1.53	2.13	1.76	2.18

Note: Censored data for individual analyses are replaced by DL/$\sqrt{2}$ (Croghan and Egeghy, 2003) in order to calculate geometric mean. Some elements have calculated geometric mean values close to or below their detection limits and thus these values are just used for reference.

[a] Samples LC15-19a and LC15-19b representing pyrite within galena (late) and pyrite within tuff (early), respectively, in the thin section LC15-19. Samples LC15-21a and LC15-21b represent coarse-grained (early) and fine-grained (late) pyrite, respectively, in the thin section LC15-21.

[b] Numbers in parenthesis representing the number of analyzed spots. *GM* = geometric mean; *GSD* = geometric standard deviation.

porphyry–skarn Mo mineralization (Yang, 2014). Lead isotopic compositions of sulfides from both types of mineralization are similar to those of the Carboniferous basalts and carbonates, and the Eocene granite porphyry ($^{206}Pb/^{204}Pb$ = 17.998–19.710, $^{207}Pb/^{204}Pb$ = 15.478–16.106, and $^{208}Pb/^{204}Pb$ = 37.870–40.115) (Ye et al., 1992; Chen et al., 2011; Zhao et al., 2012; Yang, 2014), indicating that Pb isotopic composition is equivocal in terms of Pb sources for both types of mineralization. Therefore, Pb and S isotopic compositions of sulfides cannot discriminate between Pb and S that originates from leaching of the surrounding volcanic rocks from Pb and S that is released directly from a cogenetic magma. Carbon, H, and O isotopic compositions suggest a mixed source of magmatic water and seawater for the stratabound Pb–Zn–Ag mineralization, whereas the porphyry–skarn Mo mineralization is characterized by a mixed source of magmatic and meteoric waters (Yang, 2014). Therefore, the common feature of both types of mineralization is the involvement of magmatic components in the ore-forming fluids.

The initial Os isotopic composition of pyrite can be used to trace the source of Os and, by inference, the other metals hosted in pyrite (Mathur et al., 2002; Barra et al., 2003; Cardon et al., 2008). The initial $^{187}Os/^{188}Os$ ratio from the pyrite isochron of the porphyry–skarn mineralization is 1.18 ± 0.33 (Fig. 7c), which is closer to typical crustal (1.0–1.5) than mantle (0.12–0.13) values (Walker and Morgan, 1989), indicating a dominantly crustal origin for the metals. A dominantly crustal origin for the porphyry–skarn mineralization is also supported by initial Sr and Nd isotopic compositions of 0.70777–0.70824 and 0.512170–0.512195 for the granite porphyry, respectively (Yang, 2014). Liu et al. (2015) obtained an initial $^{187}Os/^{188}Os$ ratio of 0.88 ± 0.42 for sphalerite and galena from the stratabound Pb–Zn–Ag mineralization, which also implies a dominantly crustal origin. Therefore, initial Os isotopic compositions indicate that pyrite from both the stratabound Pb–Zn–Ag and porphyry–skarn Mo mineralization is mainly crustal in origin.

6.3. Sources of the ore-forming fluids, as constrained by pyrite Se/S and Co/Ni ratios

Selenium, Co, and Ni are lattice-bound elements, as Se is able to substitute for S in the pyrite lattice, and Co and Ni are able to substitute for Fe (Abraitis et al., 2004). In this section, Se/S and Co/Ni ratios are used to constrain the sources of ore-forming fluids.

Due to the chemical similarities between S and Se, and the contrasting contents of these elements in seawater, primitive mantle, and sedimentary and volcanic rocks, Se/S ratios have been used to infer the source(s) of Se and S in ore-forming systems (Eckstrand et al., 1989; Ripley et al., 2002), particularly in VMS deposits (Huston et al., 1995a, 1995b; Gaspar, 2002; Houghton et al., 2004; Layton-Matthews et al., 2005, 2008). Seawater has a Se/S ratio of $2–10 \times 10^{-8}$ (Brewer, 1975; Measures and Burton, 1980), whereas magmatic fluids likely have Se/S ratios of $5–10 \times 10^{-5}$, similar to igneous rocks (Sindeeva, 1964). In hydrothermal fluids at temperatures above 200 °C, the dominant aqueous Se and S species are H_2Se and H_2S, respectively (D'yachkova and Khodakovkiy, 1968; Yamamoto, 1976), and thus mH_2Se/mH_2S approximates the $m\Sigma Se/m\Sigma S$ value of the hydrothermal fluid (Huston et al., 1995a, 1995b). Under these conditions, the partitioning of Se and S between a hydrothermal fluid and sulfide minerals can be recorded in the sulfides, and the $\Sigma H_2Se/\Sigma H_2S$ of the fluids can be calculated given the appropriate $K_{reaction}$ data and mineral compositions (Huston et al., 1995b). In a volcanogenic hydrothermal system, Se contents in pyrite are governed by $FeS_2 + 2H_2Se_{aq} = FeSe_2 + 2H_2S_{aq}$. For this reaction, $K_{reaction}^{1/2} = (Se/S)_{pyrite}/(mH_2Se/mH_2S)_{fluid}$ (Huston et al., 1995b), where $(Se/S)_{pyrite}$ is the molar ratio of Se and S. Assuming temperatures of 300 °C and 350 °C for the stratabound Pb–Zn–Ag and porphyry–skarn Mo mineralization (Yang, 2014), respectively, and using the method proposed by Huston et al. (1995a, 1995b), $K_{reaction}$ values of 1.11 and 0.96 are obtained and the $m\Sigma Se/m\Sigma S$ value of the hydrothermal fluid
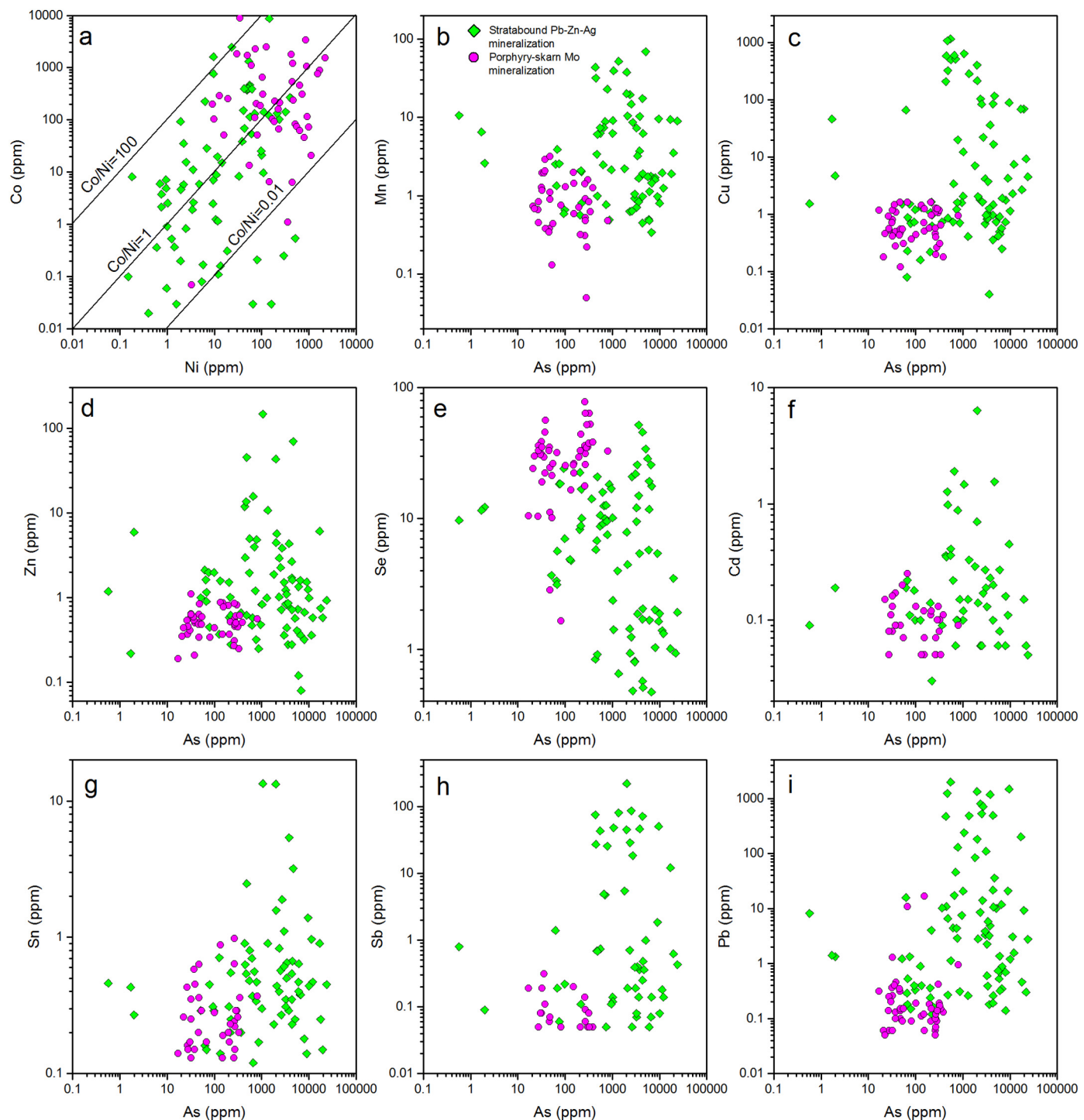
Fig. 10. Bivariate plots of selected elements in pyrite, showing the compositional differences between stratabound Pb–Zn–Ag and porphyry–skarn Mo mineralization. (a) Co versus Ni. (b–i) As versus Mn, Cu, Zn, Se, Cd, Sn, Sb, and Pb.

can be calculated (details of the calculation procedures are presented in Appendix C). Results show that fluids responsible for the stratabound Pb–Zn–Ag mineralization have $(Se/S)_{fluid}$ from 3.0×10^{-7} to 3.6×10^{-5}, with an average of 6.9×10^{-6} (Appendix B). These values lie between those of seawater and magmatic fluids, and are comparable with those of fluids for Cu-rich VMS ores from eastern Australia ($7–100 \times 10^{-6}$) that contain significant amounts of magmatic S and Se (Huston et al., 1995b). Similarly, a magmatic component may have been involved in the formation of the stratabound Pb–Zn–Ag ores at the Laochang deposit, through either the direct incorporation of

magmatic–hydrothermal fluids or by the leaching of sulfides from volcanic rocks. Fluids responsible for the porphyry–skarn Mo mineralization have $(Se/S)_{fluid}$ ratios from 1.4×10^{-6} to 6.17×10^{-5}, with an average of 2.55×10^{-5} (Appendix B), higher than those of fluids related to the stratabound Pb–Zn–Ag mineralization and similar to magmatic–hydrothermal fluids ($5–10 \times 10^{-5}$).

In addition to Se/S ratios, Co/Ni ratios of pyrite are useful in discriminating pyrite with different origins (Loftus-Hills and Solomon, 1967; Bralia et al., 1979; Bajwah et al., 1987; Gregory et al., 2015). Relatively high Co and Ni concentrations in pyrite have long been
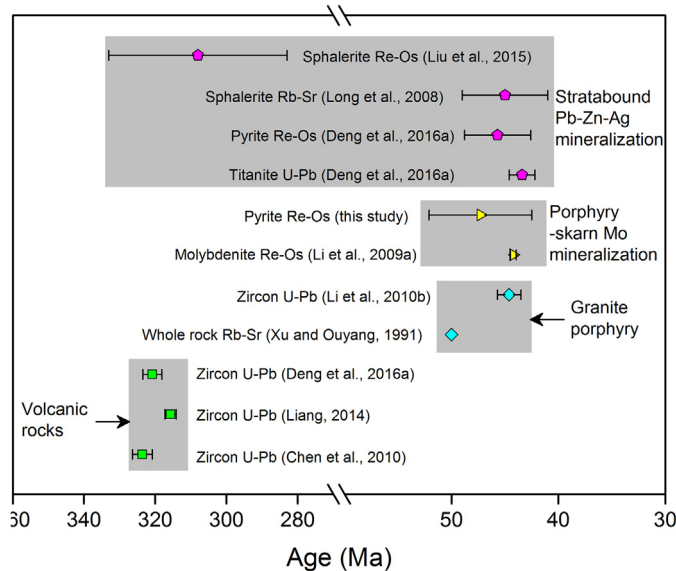
Fig. 11. Compiled age data for volcanic rocks, granite porphyry, and strata-bound Pb–Zn–Ag and porphyry–skarn mineralization in the Laochang deposit. The age errors are expressed as 2σ. Gray fields represent different types of rock or mineralization. The vertical axis denotes the samples used for dating. Data sources: Xu and Ouyang (1991); Long et al. (2008); Li et al. (2009, 2010); Chen et al. (2010); Liang (2014); Liu et al. (2015); X.-D. Deng et al. (2016); this study.

attributed to high-temperature magmatic–hydrothermal systems related to mafic sources, particularly where Co/Ni ratios are higher than unity (Bralia et al., 1979; Bajwah et al., 1987). This is in contrast to sedimentary environments where pyrite exhibits low Co/Ni ratios (Loftus-Hills and Solomon, 1967; Mookherjee and Philip, 1979; Koglin et al., 2010; Large et al., 2014).

Fig. 12 compares the Co/Ni ratios of pyrite from the Laochang deposit with those of pyrite from volcanic–hydrothermal deposits/vents (VMS deposits and submarine hydrothermal vents), sediment-hosted deposits (SEDEX deposits), sedimentary rocks, and magmatic–hydrothermal deposits (porphyry Cu and IOCG deposits). VMS deposits have relatively high and variable Co and Ni contents with Co/Ni ratios of 0.01–100. Data for VMS deposits overlap the high-Co and high-Ni pyrite grains from the stratabound Pb–Zn–Ag mineralization, and nearly all the pyrite grains from the porphyry–skarn Mo mineralization. Pyrite from submarine hydrothermal vents has highly variable Co contents and relatively constant Ni contents. The submarine hydrothermal vent data overlap those of the stratabound Pb–Zn–Ag mineralization, and partly overlap those of the porphyry–skarn mineralization (Fig. 12b). Pyrite from SEDEX deposits contains variable Co and Ni contents, with a narrow range of Co/Ni ratios (0.01–1.00) (Fig. 12c). Pyrite from both the stratabound Pb–Zn–Ag and porphyry–skarn Mo mineralization has lower Ni contents and higher Co/Ni ratios than pyrite from SEDEX deposits. Sedimentary pyrite has highly variable Co and Ni contents, with Co/Ni ratios mostly < 1 (Fig. 12d). Pyrite from porphyry Cu and IOCG deposits has a narrow range of Co and Ni contents, which overlap data for the porphyry–skarn Mo mineralization (Fig. 12e–f). Based on the above discussion, the highly variable Co and Ni contents, and Co/Ni ratios of pyrite from the stratabound Pb–Zn–Ag mineralization suggest a mixed hydrothermal and sedimentary origin. The relatively high Co and Ni contents of pyrite from the porphyry–skarn Mo mineralization are comparable with those of pyrite from porphyry Cu and IOCG deposits, indicating a magmatic–hydrothermal origin.

6.4. Genetic relationship between the stratabound Pb–Zn–Ag and porphyry–skarn mineralization

From geological observations and the data presented above, it appears unlikely that the stratabound Pb–Zn–Ag and porphyry–skarn Mo ores in the Laochang deposit are the products of a common magmatic–hydrothermal fluid. A close spatial relationship between intrusion-related Cu-Mo and stratabound Pb–Zn–Ag mineralization cannot be assumed to define a genetic or temporal relationship. This spatial relationship between intrusion-hosted Cu-Mo and stratabound Pb–Zn–Ag mineralization is not restricted to the Sanjiang Tethyan metallogenic province. Similar deposits exist in the Noranda (Quebec, Canada) (Goldie et al., 1979), Archean Panorama (Western Australia) (Brauhart et al., 1998), and Sturgeon Lake Camp (northwestern Ontario, Canada) VMS districts (Galley et al., 2000). The porphyry–skarn Mo mineralization was clearly later than the stratabound Pb–Zn–Ag mineralization at Laochang, which is inconsistent with their formation in a coeval magmatic–hydrothermal event, and suggests that their spatial coexistence may be fortuitous. Moreover, pyrite from the stratabound Pb–Zn–Ag and porphyry-skarn mineralization has different origins. Se/S and Co/Ni ratios of pyrite indicate a magmatic–hydrothermal origin for the porphyry–skarn mineralization and a mixed hydrothermal and sedimentary (seawater) origin for the stratabound Pb–Zn–Ag mineralization.

Although the stratabound Pb–Zn–Ag and porphyry–skarn mineralization at Laochang represent distinct mineralization systems with different origins, the ore fluids do share some compositional similarities. For example, sulfides from both types of mineralization have similar S-Pb isotopic compositions, which are indistinguishable from those of the Carboniferous volcanic rocks and Eocene granite porphyry. Both types of mineralization were possibly crustal in origin, as inferred from sulfide initial Os isotopic ratios. Moreover, C, H, O, and S isotopes, and pyrite Se/S and Co/Ni ratios indicate that a magmatic component was involved in the formation of the stratabound Pb–Zn–Ag ores. Huston et al. (2011) considered that two subgroups of VMS deposits have a major or dominant magmatic–hydrothermal source of ore fluids and metals. One group is characterized by high Cu and Au, and advanced aluminous argillic alteration assemblages or metamorphosed equivalents. These deposits have uniformly high salinities (~15 wt% NaCl$_{equiv.}$) or strongly ^{18}O-enriched (δ^{18}O > 5‰) ore fluids. The second group is reduced and Sn-rich, where Sn was formed at high temperatures as cassiterite. In the Laochang deposit, homogenization temperatures and salinities for the stratabound Pb–Zn–Ag mineralization are 160–356 °C and 4.6–26.3 wt% NaCl$_{equiv.}$, respectively (Li and Tian, 1995; Yang, 2014). The highly variable fluid salinities, and the absence of cogenetic subvolcanic intrusions and argillic alteration assemblages are inconsistent with an intrusion-related magmatic–hydrothermal system (e.g., porphyry Cu-Au deposits) being directly responsible for the formation of the Pb–Zn–Ag ores.

The "magmatic" signal in the stratabound Pb–Zn–Ag mineralization possibly reflects an overprint by later magmatic–hydrothermal fluids related to the Eocene granite porphyry. Identification of ~44 Ma sulfides (Long et al., 2008; X.-D. Deng et al., 2016) in the stratabound Pb–Zn–Ag ores also suggests a possible Eocene overprint. X.-D. Deng et al. (2016) showed that pyrite samples have very low Re and total Os contents of ~0.4–3.6 ppb and ~10–76 ppt, respectively, different from early sulfides with much higher Re-Os contents (Liu et al., 2015), and thus the Re-Os isochron age may represent the age of post-ore recrystallization or resetting. Different generations of pyrite in the same ore also appear to record a mixed and possibly diachronous origin. For example, in sample LC15-21, the low Se contents (0.81–3.48 ppm) and (Se/S)$_{fluid}$ values (0.6–2.6 × 10^{-6}), but high As contents (2341–23,869 ppm) for the coarse-grained pyrite indicate a sedimentary origin. However, the high Co and Ni contents (35–8731 ppm Co and 2–145 ppm Ni) of the coarse-grained pyrite are inconsistent with a sedimentary origin. This indicates that the coarse-grained pyrite formed
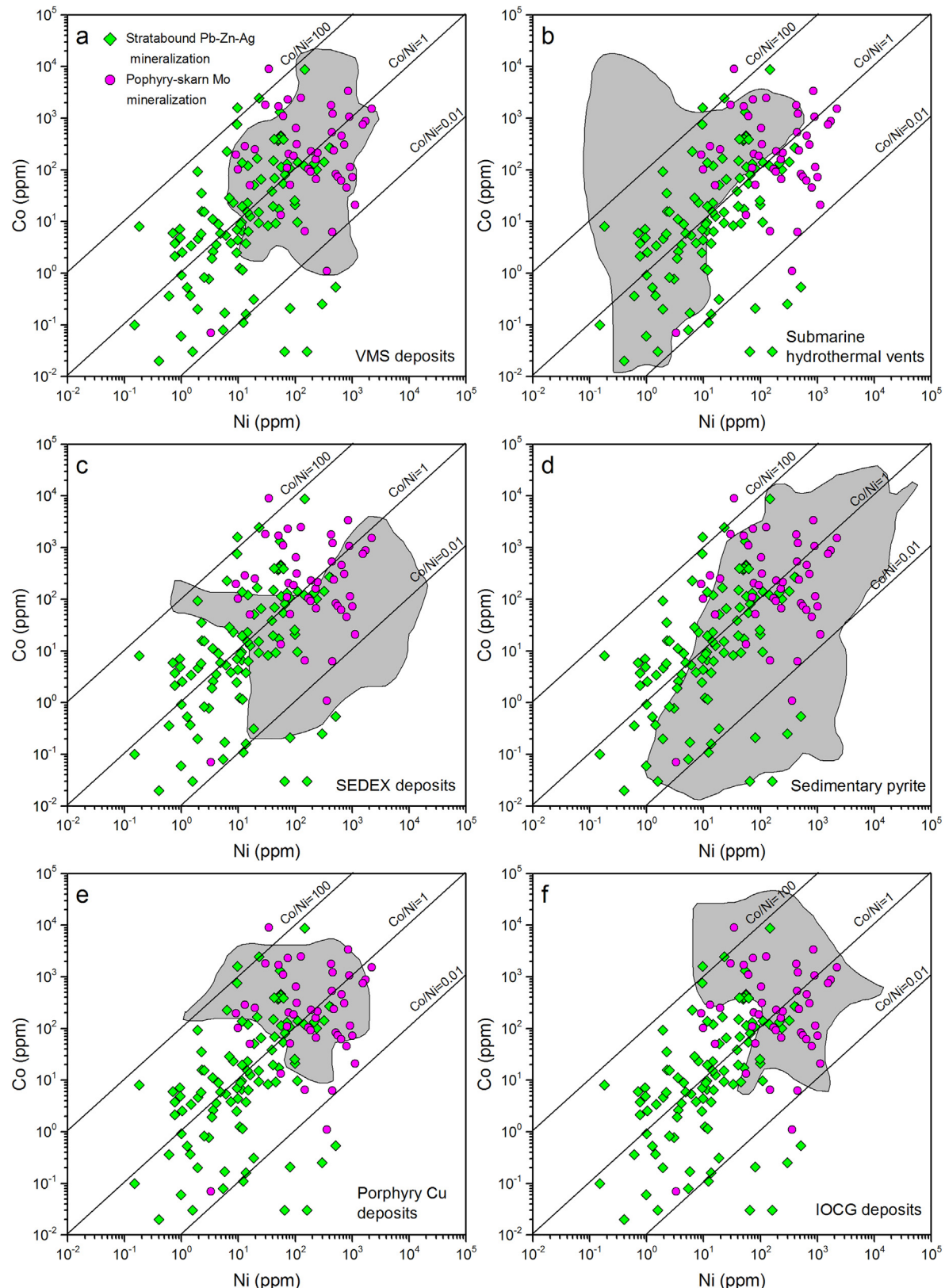
Fig. 12. Plots of Co vs. Ni contents in pyrite from the Laochang deposit. Trace element data for stratabound Pb–Zn–Ag mineralization include LA–ICP–MS data obtained in this study and solution ICP–MS data from Long et al. (2011). Microanalytical data for pyrite from other deposit/rock types are shown as gray fields. (a) VMS deposits (Keketale in Altay of NW China; Bathurst and Matagami districts of Canada; Pontide of NE Turkey) (Zheng et al., 2013; Revan et al., 2014; Genna and Gaboury, 2015; Soltani Dehnavi et al., 2015). (b) Submarine hydrothermal vents (Keith et al., 2016). (c) SEDEX deposits (Howard's Pass district of Canada; McArthur Basin of Australia) (Gadd et al., 2016; Mukherjee and Large, 2017). (d) Sedimentary pyrite (worldwide) (Berner et al., 2013; Large et al., 2014; Gregory et al., 2015; Mukherjee and Large, 2017). (e) Porphyry Cu deposits (Dexing and Jinchang of China; Metaliferi Mountains of Romania) (Deditius et al., 2013; Cioacă et al., 2014; Zhang et al., 2016). (f) IOCG deposits (Ernest Henry of Australia; Manto Verde of Chile) (Rieger et al., 2010; Rusk et al., 2010).

by the modification of sedimentary pyrite by later magmatic–hydrothermal fluids. Fine-grained pyrite has high Se contents (5.4–51.9 ppm) and $(Se/S)_{fluid}$ values ($3.8–36.1 \times 10^{-6}$), but low As contents (3647–5119 ppm). The Se contents and $(Se/S)_{fluid}$ values of the fine-grained pyrite are comparable with those of pyrite from the porphyry–skarn Mo mineralization, although with obviously higher As contents, indicating that the fine-grained pyrite also possibly originated from modification of sedimentary pyrite by later magmatic–hydrothermal fluids. Therefore, the fine- and coarse-grained pyrite possibly experienced various degrees of magmatic–hydrothermal modification, resulting in hybrid pyrite chemistries. Therefore, we suggest that the stratabound Pb–Zn–Ag and porphyry–skarn Mo mineralization represent two different mineralization systems formed in different stages and with different origins. The porphyry–skarn Mo mineralization was derived from magmatic–hydrothermal fluids associated with a granite porphyry, whereas the stratabound Pb–Zn–Ag mineralization has a mixed hydrothermal and sedimentary origin. The magmatic component in the stratabound Pb–Zn–Ag ores might reflect an overprint by later magmatic–hydrothermal activity that was responsible for porphyry–skarn Mo mineralization. The overprint is also evidenced by characteristic phyllic and propylitization alteration around the stratabound Pb–Zn–Ag orebodies (Fig. 2), which is a common style of alteration in porphyry base-metal systems (e.g., Sillitoe, 2010). Moreover, calcite-quartz ± sulfide veins are very common in tuff and altered volcanic rocks around sulfide orebody (Fig. 3d–e), implying extensive hydrothermal activities after volcanism. Particularly, part of stratabound sulfide orebody was crosscut or replaced by calcite-quartz ± sulfide veins (Fig. 3f–g), which may result in the remobilization of metals in massive sulfide ores.

The overprinting model is consistent with the regional tectonic evolution. In the early Carboniferous, rift volcanism was extensive in the Lancang area (Metcalfe, 2013; Li et al., 2015). Hydrothermal fluids accompanying volcanism were transferred from the deep crust to the seafloor along inherited magma pathways and faults, which formed the stratabound Pb–Zn–Ag orebodies. Multiple volcanic eruptions and related hydrothermal activity resulted in multiple sulfide orebodies. From the Permian to Triassic, the tectonic setting of the Lancang area changed from extensional to compressional (Metcalfe, 2013) and the stratabound Pb–Zn–Ag orebodies experienced intense deformation. In the Eocene, collisional tectonics and orogenesis were dominant in this area (Deng et al., 2014), and the orebodies were subjected to further deformation and exhumation. Extensive granitic magmatism and associated hydrothermal activity were associated with these events, which resulted in the formation of porphyry–skarn Mo mineralization proximal to the intrusions. Hydrothermal fluids continued to move up and replaced/remobilized the former stratabound Pb–Zn–Ag ores, resulting in the formation of new ores with hybrid origins. It is difficult to quantitatively evaluate the extent of overprinting because the overprint is variable in different ores or locations. However, we can qualitatively evaluate the overprint texturally. Approximately 30% of the studied ores show obvious replacement textures (Fig. 4d), which are different from the typical textures of VMS ores such as turbidites from sulfide mounds (Fig. 4j). Therefore, we infer that nearly one-third of the stratabound Pb–Zn–Ag ores have been remobilized by post-ore fluids, although this estimate needs further refinement.

7. Conclusions

Pyrite from the Laochang porphyry–skarn Mo mineralization yields a Re-Os isochron age of 47.3 ± 4.8 Ma, consistent with a previously published molybdenite Re-Os age. The initial Os isotopic composition of the pyrite indicates a dominantly crustal origin for the porphyry–skarn Mo mineralization, similar to that for the stratabound Pb–Zn–Ag mineralization. Sulfur isotopic compositions of the sulfides indicate a similar magmatically derived sulfur source for both types of mineralization. Trace element compositions of pyrite (Se/S and Co/Ni) imply

a mixed sedimentary and hydrothermal origin for the stratabound Pb–Zn–Ag mineralization, and a magmatic–hydrothermal origin for the porphyry–skarn Mo mineralization. Identification of Eocene Pb–Zn–Ag mineralization and the hydrothermal and sedimentary origins of pyrite in the stratabound Pb–Zn–Ag ores indicate that the magmatic–hydrothermal component in these ores reflects an overprint of Carboniferous VMS mineralization by magmatic–hydrothermal fluids related to the Eocene granite porphyry. We consider that the stratabound Pb–Zn–Ag and porphyry–skarn mineralizations in the Laochang deposit represent two different mineralization systems, and the former appears to have been overprinted by the latter.

Supplementary data to this article can be found online at https://doi.org/10.1016/j.gexplo.2018.08.008.

References

Abraitis, P.K., Pattrick, R.A.D., Vaughan, D.J., 2004. Variations in the compositional, textural and electrical properties of natural pyrite: a review. Int. J. Miner. Process. 74, 41–59.

Bajwah, Z.U., Seccombe, P.K., Offler, R., 1987. Trace element distribution, Co: Ni ratios and genesis of the Big Cadia iron-copper deposit, New South Wales, Australia. Mineral. Deposita 22, 292–300.

Barra, F., Ruiz, J., Mathur, R., Titley, S., 2003. A Re-Os study of sulfide minerals from the Bagdad porphyry Cu-Mo deposit, northern Arizona, USA. Miner. Deposita 38, 585–596.

Barra, F., Reich, M., Selby, D., Rojas, P., Simon, A., Salazar, E., Palma, G., 2017. Unraveling the origin of the Andean IOCG clan: a Re-Os isotope approach. Ore Geol. Rev. 81, 62–78.

Berner, Z.A., Puchelt, H., Noeltner, T., Kramar, U.T.Z., 2013. Pyrite geochemistry in the Toarcian Posidonia Shale of south-west Germany: evidence for contrasting trace-element patterns of diagenetic and syngenetic pyrites. Sedimentology 60, 548–573.

Bralia, A., Sabatini, G., Troja, F., 1979. A revaluation of the Co/Ni ratio in pyrite as geochemical tool in ore genesis problems. Miner. Deposita 14, 353–374.

Brauhart, C.W., Groves, D.I., Morant, P., 1998. Regional alteration systems associated with volcanogenic massive sulfide mineralization at Panorama, Pilbara, Western Australia. Econ. Geol. 93, 292–302.

Brewer, P.G., 1975. Minor elements in seawater. In: Riley, J.P., Skirrow, G. (Eds.), Chemical Oceanography, 2nd ed. Academic Press, London.

Burchfiel, B.C., Chen, Z., 2012. Tectonics of the southeastern Tibetan Plateau and its adjacent foreland. Geol. Soc. Am. Bull. 210, 1–164.

Cardon, O., Reisberg, L., Andre-Mayer, A.S., Leroy, J., Milu, V., Zimmermann, C., 2008. Re-Os systematics of pyrite from the Bolcana porphyry copper deposit, Apuseni mountains, Romania. Econ. Geol. 103, 1695–1702.

Chen, M., Huang, Z.L., Luo, T.Y., Yan, Z.F., Long, H.S., 2010. SHRIMP dating and its geological significance of zircon in volcanic from Laochang large silver-lead-zinc deposit in Western Yunnan Province, China. Acta Mineral. Sin. 30, 456–462 (in Chinese with English abstract).

Chen, M., Huang, Z.L., Luo, T.Y., Yan, Z.F., Long, H.S., 2011. Petrogenesis and tectonic significance of the Laochang basalt in western Yunnan Province, China. Acta Mineral. Sin. 31, 55–61 (in Chinese with English abstract).

Cioacă, M.E., Munteanu, M., Qi, L., Costin, G., 2014. Trace element concentrations in porphyry copper deposits from Metaliferi Mountains, Romania: a reconnaissance study. Ore Geol. Rev. 63, 22–39.

Cook, N.J., Ciobanu, C.L., Mao, J., 2009. Textural control on gold distribution in As-free pyrite from the Dongping, Huangtuliang and Hougou gold deposits, North China Craton (Hebei Province, China). Chem. Geol. 264, 101–121.

Croghan, C., Egeghy, P.P., 2003. Methods of dealing with values below the limit of detection using SAS. 22. Southern SAS User Group, pp. 24.

Deditius, A.P., Utsunomiya, S., Renock, D., Ewing, R.C., Ramana, C.V., Becker, U., Kesler, S.E., 2008. A proposed new type of arsenian pyrite: Composition, nanostructure and geological significance. Geochim. Cosmochim. Acta 72, 2919–2933.

Deditius, A., Chryssoulis, S., Li, J.W., Ma, C.Q., Parada Reyes, M., Barra, F., Reich

Morales, M., Mittermayr, F., 2013. Pyrite as a record of hydrothermal fluid evolution in a porphyry copper system: a SIMS/EMPA trace element study. Geochim. Cosmochim. Acta 104, 42–62.

Deng, J., Wang, Q., Li, G., Santosh, M., 2014. Cenozoic tectono-magmatic and metallogenic processes in the Sanjiang region, southwestern China. Earth Sci. Rev. 138, 268–299.

Deng, X.-D., Li, J.-W., Zhao, X.-F., Wang, H.-Q., Qi, L., 2016. Re–Os and U–Pb geochronology of the Laochang Pb–Zn–Ag and concealed porphyry Mo mineralization along the Changning–Menglian suture, SW China: implications for ore genesis and porphyry Cu–Mo exploration. Miner. Deposita 51, 237–248.

Deng, X.-H., Wang, J.-B., Pirajno, F., Wang, Y.-W., Li, Y.-C., Li, C., Zhou, L.-M., Chen, Y.-J., 2016. Re–Os dating of chalcopyrite from selected mineral deposits in the Kalatag district in the eastern Tianshan Orogen, China. Ore Geol. Rev. 77, 72–81.

Ding, T.P., Vaikiers, S., Wan, D.F., Bai, R.M., Zou, X.Q., Li, Y.H., Zhang, Q.L., Bievre, P.D., 2001. The $\delta^{33}S$ and $\delta^{34}S$ values and absolute $^{32}S/^{33}S$ and $^{32}S/^{34}S$ ratios of IAEA and chinese sulfur isotope reference materials. Bull. China Soc. Mineral. Petrol. Geochem. 20, 425–427 (in Chinese with English abstract).

D'yachkova, I.B., Khodakovkiy, I.L., 1968. Thermodynamic equilibria in the systems S-H_2O, Se-H_2O and Te-H_2O in the 25–300 °C temperature range and their geochemical interpretations. Geochem. Int. 5, 1108–1112.

Eckstrand, O.R., Grinenko, L.N., Krouse, H.R., Paktunc, A.D., Schwann, P.L., Scoates, R.F.J., 1989. Preliminary data on sulphur isotopes and Se/S ratios, and the source of sulphur in magmatic sulphides from the Fox River Sill, Molson Dykes and Thompson nickel deposits, northern Manitoba. In: Current Research Part C, Geological Survey of Canada, pp. 235–242.

Gadd, M.G., Layton-Matthews, D., Peter, J.M., Paradis, S.J., 2016. The world-class Howard's Pass SEDEX Zn-Pb district, Selwyn Basin, Yukon. Part I: trace element compositions of pyrite record input of hydrothermal, diagenetic, and metamorphic fluids to mineralization. Miner. Deposita 51, 319–342.

Galley, A., van Breemen, O., Franklin, J., 2000. The relationship between intrusion-hosted Cu-Mo mineralization and the VMS deposits of the Archean Sturgeon Lake mining camp, northwestern Ontario. Econ. Geol. 95, 1543–1550.

Gao, J.-F., Jackson, S.E., Dubé, B., Kontak, D.J., De Souza, S., 2015. Genesis of the Canadian Malartic, Côté Gold, and Musselwhite gold deposits: insights from LA-ICP-MS element mapping of pyrite. In: Dubé, B., Mercier-Langevin, P. (Eds.), Targeted Geoscience Initiative 4: Contributions to the Understanding of Precambrian Lode Gold Deposits and Implications for Exploration, pp. 157–175 (Geological Survey of Canada Open File 7852).

Gaspar, O.C., 2002. Mineralogy and sulfide mineral chemistry of the Neves–Corvo ores, Portugal: insight into their genesis. Can. Mineral. 40, 611–636.

Genna, D., Gaboury, D., 2015. Deciphering the hydrothermal evolution of a VMS system by LA-ICP-MS using trace elements in pyrite: an example from the Bracemac-McLeod deposits, Abitibi, Canada, and implications for exploration. Econ. Geol. 110, 2087–2108.

Goldie, R., Kotila, B., Seward, D., 1979. The Don Rouyn Mine: an Archean porphyry copper deposit near Noranda, Quebec. Econ. Geol. 74, 1680–1684.

Gregory, D., Meffre, S., Large, R., 2014. Comparison of metal enrichment in pyrite framboids from a metal-enriched and metal-poor estuary. Am. Mineral. 99, 633–644.

Gregory, D.D., Large, R.R., Halpin, J.A., Baturina, E.L., Lyons, T.W., Wu, S., Danyushevsky, L., Sack, P.J., Chappaz, A., Maslennikov, V.V., 2015. Trace element content of sedimentary pyrite in black shales. Econ. Geol. 110, 1389–1410.

Gregory, D.D., Large, R.R., Bath, A.B., Steadman, J.A., Wu, S., Danyushevsky, L., Bull, S.W., Holden, P., Ireland, T.R., 2016. Trace Element Content of Pyrite from the Kapai Slate, St. Ives Gold District, Western Australia. Econ. Geol. 111, 1297–1320.

Halicz, L., Günther, D., 2004. Quantitative analysis of silicates using LA-ICP-MS with liquid calibration. J. Anal. At. Spectrom. 19, 1539–1545.

Hnatyshin, D., Creaser, R.A., Wilkinson, J.J., Gleeson, S.A., 2015. Re-Os dating of pyrite confirms an early diagenetic onset and extended duration of mineralization in the Irish Zn-Pb ore field. Geology 43, 143–146.

Hnatyshin, D., Kontak, D.J., Turner, E.C., Creaser, R.A., Morden, R., Stern, R.A., 2016. Geochronologic (Re-Os) and fluid-chemical constraints on the formation of the Mesoproterozoic-hosted Nanisivik Zn-Pb deposit, Nunavut, Canada: evidence for early diagenetic, low-temperature conditions of formation. Ore Geol. Rev. 79, 189–217.

Hou, Z., Zeng, P., Gao, Y., Du, A., Fu, D., 2006. Himalayan Cu–Mo–Au mineralization in the eastern Indo–Asian collision zone: constraints from Re–Os dating of molybdenite. Miner. Deposita 41, 33–45.

Hou, Z., Zaw, K., Pan, G., Mo, X., Xu, Q., Hu, Y., Li, X., 2007. Sanjiang Tethyan metallogenesis in SW China: Tectonic setting, metallogenic epochs and deposit types. Ore Geol. Rev. 31, 48–87.

Houghton, J., Shanks, W., Seyfried, W., 2004. Massive sulfide deposition and trace element remobilization in the Middle Valley sediment-hosted hydrothermal system, northern Juan de Fuca Rdge. Geochim. Cosmochim. Acta 68, 2863–2873.

Huang, X.-W., Qi, L., Gao, J.-F., Zhou, M.-F., 2013a. First reliable Re-Os ages of pyrite and stable isotope compositions of Fe(-Cu) deposits in the Hami region, Eastern Tianshan Orogenic Belt, NW China. Resour. Geol. 63, 166–187.

Huang, X.-W., Zhao, X.-F., Qi, L., Zhou, M.-F., 2013b. Re-Os and S isotopic constraints on the origins of two mineralization events at the Tangdan sedimentary rock-hosted stratiform Cu deposit, SW China. Chem. Geol. 347, 9–19.

Huang, X.-W., Zhou, M.-F., Qi, L., Gao, J.-F., Wang, Y.-W., 2013c. Re-Os isotopic ages of pyrite and chemical composition of magnetite from the Cihai magmatic-hydrothermal Fe deposit, NW China. Miner. Deposita 48, 925–946.

Huang, X.-W., Gao, J.-F., Qi, L., Zhou, M.-F., 2015. In-situ LA-ICP-MS trace elemental analyses of magnetite and Re–Os dating of pyrite: the Tianhu hydrothermally remobilized sedimentary Fe deposit, NW China. Ore Geol. Rev. 65, 900–916.

Huston, D.L., Sie, S.H., Suter, G.F., 1995a. Selenium and its importance to the study of ore genesis: the theoretical basis and its application to volcanic-hosted massive sulfide deposits using pixeprobe analysis. Nucl. Instrum. Methods Phys. Res., Sect. B 104, 476–480.

Huston, D.L., Sie, S.H., Suter, G.F., Cooke, D.R., Both, R.A., 1995b. Trace elements in sulfide minerals from eastern Australian volcanic-hosted massive sulfide deposits; part I, proton microprobe analyses of pyrite, chalcopyrite, and sphalerite, and part II, selenium levels in pyrite; comparison with $\delta^{34}S$ values and implications for the source of sulfur in volcanogenic hydrothermal systems. Econ. Geol. 90, 1167–1196.

Huston, D.L., Relvas, J.M., Gemmell, J.B., Drieberg, S., 2011. The role of granites in volcanic-hosted massive sulphide ore-forming systems: an assessment of magmatic–hydrothermal contributions. Miner. Deposita 46, 473–507.

Ingham, E.S., Cook, N.J., Cliff, J., Ciobanu, C.L., Huddleston, A., 2014. A combined chemical, isotopic and microstructural study of pyrite from roll-front uranium deposits, Lake Eyre Basin, South Australia. Geochim. Cosmochim. Acta 125, 440–465.

Jian, P., Liu, D., Kröner, A., Zhang, Q., Wang, Y., Sun, X., Zhang, W., 2009. Devonian to Permian plate tectonic cycle of the Paleo-Tethys Orogen in southwest China (II): insights from zircon ages of ophiolites, arc/back-arc assemblages and within-plate igneous rocks and generation of the Emeishan CFB province. Lithos 113, 767–784.

Keith, M., Häckel, F., Haase, K.M., Schwarz-Schampera, U., Klemd, R., 2016. Trace element systematics of pyrite from submarine hydrothermal vents. Ore Geol. Rev. 72, 728–745.

Kelley, K.D., Selby, D., Falck, H., Slack, J.F., 2017. Re-Os systematics and age of pyrite associated with stratiform Zn-Pb mineralization in the Howards Pass district, Yukon and Northwest Territories, Canada. Mineral. Deposita 52, 317–335.

Koglin, N., Frimmel, H.E., Minter, W.L., Brätz, H., 2010. Trace-element characteristics of different pyrite types in Mesoarchaean to Palaeoproterozoic placer deposits. Miner. Deposita 45, 259–280.

Lambert, D.D., Foster, J.G., Frick, L.R., Li, C., Naldrett, A.J., 1999. Re-Os isotopic systematics of the Voisey's bay Ni-Cu-Co magmatic ore system, Labrador, Canada. Lithos 47, 69–88.

Large, R.R., Danyushevsky, L., Hollit, C., Maslennikov, V., Meffre, S., Gilbert, S., Bull, S., Scott, R., Emsbo, P., Thomas, H., 2009. Gold and trace element zonation in pyrite using a laser imaging technique: implications for the timing of gold in orogenic and Carlin-style sediment-hosted deposits. Econ. Geol. 104, 635–668.

Large, R.R., Halpin, J.A., Danyushevsky, L.V., Maslennikov, V.V., Bull, S.W., Long, J.A., Gregory, D.D., Lounejeva, E., Lyons, T.W., Sack, P.J., 2014. Trace element content of sedimentary pyrite as a new proxy for deep-time ocean–atmosphere evolution. Earth Planet. Sci. Lett. 389, 209–220.

Large, R.R., Gregory, D.D., Steadman, J.A., Tomkins, A.G., Lounejeva, E., Danyushevsky, L.V., Halpin, J.A., Maslennikov, V., Sack, P.J., Mukherjee, I., 2015. Gold in the oceans through time. Earth Planet. Sci. Lett. 428, 139–150.

Layton-Matthews, D., Scott, S.D., Peter, J.M., Leybourne, M.I., 2005. Transport and deposition of selenium in felsic volcanic-hosted massive sulfide deposits of the Finlayson Lake District, Yukon Territory, Canada. In: Mao, J., Bierlein, F.P. (Eds.), Mineral Deposit Research: Meeting the Global Challenge. Springer, Berlin, Heidelberg, pp. 643–646.

Layton-Matthews, D., Peter, J.M., Scott, S.D., Leybourne, M.I., 2008. Distribution, mineralogy, and geochemistry of selenium in felsic volcanic-hosted massive sulfide deposits of the Finlayson Lake district, Yukon Territory, Canada. Econ. Geol. 103, 61–88.

Li, Y., Liu, J., 2006. Calculation of sulfur isotope fractionation in sulfides. Geochim. Cosmochim. Acta 70, 1789–1795.

Li, H.J., Tian, X., 1995. The study on fluid inclusion and its ore-forming physicochemical conditions for Langcang Pb-Zn-Ag-Cu deposit. Mineral Resour. Geol. 9, 107–111 (in Chinese with English abstract).

Li, H.J., Tian, X., Yi, F.C., 1995. The stable isotope geochemistry of the Lancang Pb-Ag-Zn-Cu deposit in Yunnan Province. Geol. Explor. Nonferrous Met. 4, 278–282 (in Chinese with English abstract).

Li, L., Duan, J.R., Li, F., Ma, Y., Huang, D.Y., 1996. Geologic features and multiperiodic syntopogeneic metallogenesis of the Laochang Cu-polymetal deposit in Lancang, Yunnan. Yunan Geol. 15, 246–256 (in Chinese with English abstract).

Li, F., Lu, W.J., Yang, Y.Z., Chen, H., Luo, S.L., Shi, Z.L., 2009a. The rock- and ore-forming ages of the Laochang porphyry molybdenite deposit in Lancang, Yunnan. Geoscience 23, 1049–1055 (in Chinese with English abstract).

Li, F., Lu, W.J., Yang, Y.Z., Chen, H., Shi, Z.L., Liu, S.W., Xin, R., Luo, S.L., 2009b. Mineralizing texture and metallogenic model of the Laochang polymetallic deposit in Lancang, Yunnan. Geol. Explor. 45, 516–523 (in Chinese with English abstract).

Li, F., Chen, H., Lu, W.J., Luo, S.L., 2010a. Rock-forming ages of the Laochang granite-porphyry, Lancang, Yunnan and their geological significance. Geotecton. Metallog. 34, 84–91 (in Chinese with English abstract).

Li, F., Lu, W.J., Yang, Y.Z., Tang, X.P., Shi, Z.L., 2010b. The Research of Crisis Miners Ore-forming Regularity and Prospecting: Take Laochang Deposit in Lancang of Yunnan as an Example. Yunnan Science and Technology Press, Kunming (in Chinese).

Li, G., Deng, J., Wang, Q., Liang, K., 2015. Metallogenic model for the Laochang Pb–Zn–Ag–Cu volcanogenic massive sulfide deposit related to a Paleo-Tethys OIB-like volcanic center, SW China. Ore Geol. Rev. 70, 578–594.

Li, D., Chen, H., Hollings, P., Zhang, L., Mi, M., Li, J., Fang, J., Wang, C., Lu, W., 2016. Re-Os pyrite geochronology of Zn-Pb mineralization in the giant Caixiashan deposit, NW China. Mineral. Deposita 51, 309–317.

Liang, K., 2014. Geochemical Characteristics and Metallogenic Model Study of Laochang VMS Pb-Zn Polymetallic Deposit, Western Yunnan Province. China University of Geosciences, Beijing, pp. 1–122 (in Chinese with English abstract).

Liu, Y., Hu, Z., Gao, S., Günther, D., Xu, J., Gao, C., Chen, H., 2008. In situ analysis of major and trace elements of anhydrous minerals by LA-ICP-MS without applying an internal standard. Chem. Geol. 257, 34–43.

Liu, Y., Qi, L., Gao, J., Ye, L., Huang, Z., Zhou, J., 2015. Re-Os dating of galena and

sphalerite from lead-zinc sulfide deposits in Yunnan Province, SW China. J. Earth Sci. 26, 343–351.

Loftus-Hills, G., Solomon, M., 1967. Cobalt, nickel and selenium in sulphides as indicators of ore genesis. Miner. Deposita 2, 228–242.

Long, H.S., Luo, T.Y., Chen, F.K., Huang, Z.L., Zhou, M.Z., Yang, Y., Qian, Z.K., 2008. Single grain sphalerite and pyrite Rb-Sr geochronology: implication for timing constraint on Ag-polymetallic Laochang deposit, Lancang, Yunnan. Bull. China Soc. Mineral. Petrol. Geochem. 27, 322–323 (in Chinese).

Long, H.S., Luo, T.Y., Huang, Z.L., Zhou, M.Z., Yang, Y., Qian, Z.K., 2011. Rare earth element and trace element geochemistry of pyrite ores in the Laochang large size silver ploymetallic deposit of Lancang, Yunnan Province, China. Acta Mineral. Sin. 31, 462–473 (in Chinese with English abstract).

Ludwig, K.R., 1980. Calculation of uncertainties of U-Pb isotope data. Earth Planet. Sci. Lett. 46, 212–220.

Ludwig, K.R., 2003. Isoplot/Ex version 3.23. A geochronological toolkit for Microsoft Excel. Berkeley Geochronology Center Special Publication.

Mao, J., Pirajno, F., Lehmann, B., Luo, M., Berzina, A., 2014. Distribution of porphyry deposits in the Eurasian continent and their corresponding tectonic settings. J. Asian Earth Sci. 79, 576–584.

Mathur, R., Ruiz, J., Titley, S., Gibbins, S., Martogomo, W., 2000. Different crustal sources for Au-rich and Au-poor ores of the Grasberg Cu-Au porphyry deposit. Earth Planet. Sci. Lett. 183, 7–14.

Mathur, R., Marschik, R., Ruiz, J., Munizaga, F., Leveille, R.A., Martin, W., 2002. Age of mineralization of the Candelaria Fe oxide Cu-Au deposit and the origin of the Chilean iron belt, based on Re-Os isotopes. Econ. Geol. 97, 59–71.

Measures, C.I., Burton, J.D., 1980. The vertical distribution and oxidation states of dissolved selenium in the northeast Atlantic Ocean and their relationship to biological processes. Earth Planet. Sci. Lett. 46, 385–396.

Metcalfe, I., 2013. Gondwana dispersion and Asian accretion: tectonic and palaeogeographic evolution of eastern Tethys. J. Asian Earth Sci. 66, 1–33.

Mo, X.X., Lu, F.X., Shen, S.Y., 1993. Sanjiang Tethyan Volcanism and Related Mineralization. Geological Publishing House, Beijing (in Chinese with English abstract).

Mookherjee, A., Philip, R., 1979. Distribution of copper, cobalt and nickel in ores and host-rocks, Ingladhal, Karnataka, India. Miner. Deposita 14, 33–55.

Morelli, R.M., Creaser, R.A., 2006. Re-Os geochronology of low-level sulfide minerals: applications and limitations. Geochim. Cosmochim. Acta 70, A429.

Morelli, R.M., Creaser, R.A., Selby, D., Kelley, K.D., Leach, D.L., King, A.R., 2004. Re-Os sulfide geochronology of the Red Dog sediment-hosted Zn-Pb-Ag deposit, Brooks Range, Alaska. Econ. Geol. 99, 1569–1576.

Mukherjee, I., Large, R., 2017. Application of pyrite trace element chemistry to exploration for SEDEX style Zn-Pb deposits: McArthur Basin, Northern Territory, Australia. Ore Geol. Rev. 81, 1249–1270.

Ohmoto, H., Rye, R.O., 1979. Isotopes of sulfur and carbon. In: Barnes, H.L. (Ed.), Geochemistry of Hydrothermal Ore Deposits. Wiley, New York, pp. 509–567.

Ouyang, C.P., Xu, C., 1991. Geochemical features and genesis of the Laochang Diwa-type silver-lead ore deposit in Langchang, Yunnan, China. Geotecton. Metallog. 15, 317–326 (in Chinese with English abstract).

Qi, L., Zhou, M.-F., Wang, C.Y., Sun, M., 2007. Evaluation of a technique for determining Re and PGEs in geological samples by ICP-MS coupled with a modified Carius tube digestion. Geochem. J. 41, 407–414.

Qi, L., Zhou, M.-F., Gao, J., Zhao, Z., 2010. An improved Carius tube technique for determination of low concentrations of Re and Os in pyrites. J. Anal. At. Spectrom. 25, 585–589.

Qi, L., Gao, J.-F., Zhou, M.-F., Hu, J., 2013. The design of re-usable Carius tubes for the determination of rhenium, osmium and platinum-group elements in geological samples. Geostand. Geoanal. Res. 37, 345–351.

Reich, M., Deditius, A., Chryssoulis, S., Li, J.-W., Ma, C.-Q., Parada, M.A., Barra, F., Mittermayr, F., 2013. Pyrite as a record of hydrothermal fluid evolution in a porphyry copper system: A SIMS/EMPA trace element study. Geochim. Cosmochim. Acta 104, 42–62.

Reich, M., Simon, A.C., Deditius, A., Barra, F., Chryssoulis, S., Lagas, G., Tardani, D., Knipping, J., Bilenker, L., Sánchez-Alfaro, P., 2016. Trace element signature of pyrite from the Los Colorados iron oxide-apatite (IOA) deposit, Chile: a missing link between Andean IOA and iron oxide copper-gold systems? Econ. Geol. 111, 743–761.

Revan, M.K., Genç, Y., Maslennikov, V.V., Maslennikova, S.P., Large, R.R., Danyushevsky, L.V., 2014. Mineralogy and trace-element geochemistry of sulfide minerals in hydrothermal chimneys from the Upper-Cretaceous VMS deposits of the eastern Pontide orogenic belt (NE Turkey). Ore Geol. Rev. 63, 129–149.

Rieger, A.A., Marschik, R., Díaz, M., Hölzl, S., Chiaradia, M., Akker, B., Spangenberg, J.E., 2010. The hypogene iron oxide copper-gold mineralization in the Mantoverde district, Northern Chile. Econ. Geol. 105, 1271–1299.

Ripley, E.M., Li, C., Shin, D., 2002. Paragneiss assimilation in the genesis of magmatic Ni-Cu-Co sulfide mineralization at Voisey's Bay, Labrador: $\delta^{34}S$, $\delta^{13}C$, and Se/S evidence. Econ. Geol. 97, 1307–1318.

Ruiz, J., Mathur, R., 1999. Metallogenesis in continental margins: Re-Os evidence from porphyry copper deposits in Chile. In: Lambert, D.D., Ruiz, J. (Eds.), Application of Radiogenic Isotopes to Ore Deposit Research and Exploration. Rev. Econ. Geol.pp. 59–72.

Rusk, B., Oliver, N., Cleverley, J., Blenkinsop, T., Zhang, D., Williams, P., Habermann, P., 2010. Physical and chemical characteristics of the Ernest Henry iron oxide copper gold deposit, Australia; implications for IOCG genesis. In: Porter, T.M. (Ed.), Hydrothermal Iron Oxide Copper-Gold & Related Deposits: A Global Perspective. PGC Publishing, Adelaide, pp. 1–18.

Sakai, H., 1968. Isotopic properties of sulfur compounds in hydrothermal processes. Geochem. J. 2, 29–49.

Schoenberg, R., Nägler, T.F., Kramers, J.D., 2000. Precise Os isotope ratio and Re-Os isotope dilution measurements down to the picogram level using multicollector inductively coupled plasma mass spectrometry. Int. J. Mass Spectrom. 197, 85–94.

Selby, D., Kelley, K.D., Hitzman, M.W., Zieg, J., 2009. Re-Os sulfide (bornite, chalcopyrite, and pyrite) systematics of the carbonate-hosted copper deposits at Ruby Creek, southern Brooks range, Alaska. Econ. Geol. 104, 437–444.

Sillitoe, R.H., 2010. Porphyry copper systems. Econ. Geol. 105, 3–41.

Sindeeva, N.D., 1964. Mineralogy and Types of Deposits of Selenium and Tellurium. Interscience Publishers, New York.

Soltani Dehnavi, A., Lentz, D.R., McFarlane, C.R.M., 2015. LA-ICP-MS analysis of volatile trace elements in massive sulphides and host rocks of selected VMS deposits of the Bathurst mining camp, New Brunswick: Methodology and application to exploration. In: Peter, J.M., Mercier-Langevin, P. (Eds.), Targeted Geoscience Initiative 4: Contributions to the Understanding of Volcanogenic Massive Sulphide Deposit Genesis and Exploration Methods Development. Geological Survey of Canada Open File 7853, pp. 59–80.

Spry, P.G., Mathur, R.D., Bonsall, T.A., Voudouris, P.C., Melfos, V., 2014. Re–Os isotope evidence for mixed source components in carbonate-replacement Pb–Zn–Ag deposits in the Lavrion district, Attica, Greece. Mineral. Petrol. 108, 503–513.

Stein, H.J., Morgan, J.W., Schersténn, A., 2000. Re-Os dating of Low-Level Highly Radiogenic (LLHR) sulfides: the Harnäs gold deposit, southwest Sweden, records continental-scale tectonic events. Econ. Geol. 95, 1657–1671.

Tanner, D., Henley, R.W., Mavrogenes, J.A., Holden, P., 2016. Sulfur isotope and trace element systematics of zoned pyrite crystals from the El Indio Au–Cu–Ag deposit, Chile. Contrib. Mineral. Petrol. 171, 1–17.

Tardani, D., Reich, M., Deditius, A.P., Chryssoulis, S., Sánchez-Alfaro, P., Wrage, J., Roberts, M.P., 2017. Copper–arsenic decoupling in an active geothermal system: a link between pyrite and fluid composition. Geochim. Cosmochim. Acta 204, 179–204.

Tristá-Aguilera, D., Barra, F., Ruiz, J., Morata, D., Talavera-Mendoza, O., Kojima, S., Ferraris, F., 2006. Re-Os isotope systematics for the Lince-Estefanía deposit: constraints on the timing and source of copper mineralization in a stratabound copper deposit, Coastal Cordillera of Northern Chile. Mineral. Deposita 41, 99–105.

Walker, R.J., Morgan, J.W., 1989. Rhenium-osmium isotope systematics of carbonaceous chondrites. Science 243, 519–522.

Wang, Z.R., Huang, Z., Peng, S.L., Chen, S.L., Hu, X.Z., 1997. Genesis and metallogenic model of Laochang-type silver multimetal massive sulfide deposits in Lancang, Yunan Province. Chin. J. Nonfer. Met. 7, 1–6 (in Chinese with English abstract).

Wang, D., Qu, W., Li, Z., Yin, H., Chen, Y., 2005. Mineralization episode of porphyry copper deposits in the Jinshajiang-Red River mineralization belt: Re-Os dating. Sci. China Ser. D Earth Sci. 48, 192–198.

Wang, C., Deng, J., Zhang, S., Yang, L., 2010. Metallogenic province and large scale mineralization of volcanogenic massive sulfide deposits in China. Resour. Geol. 60, 404–413.

Wang, B., Wang, L., Pan, G., Yin, F., Wang, D., Tang, Y., 2013. U-Pb zircon dating of Early Paleozoic gabbro from the Nantinghe ophiolite in the Changning-Menglian suture zone and its geological implication. Chin. Sci. Bull. 58, 920–930.

Xiong, Y., Wood, S.A., 1999. Experimental determination of the solubility of ReO_2 and the dominant oxidation state of rhenium in hydrothermal solutions. Chem. Geol. 158, 245–256.

Xiong, Y., Wood, S., Kruszewski, J., 2006. Hydrothermal transport and deposition of rhenium under subcritical conditions revisited. Econ. Geol. 101, 471–478.

Xu, C., Ouyang, C.P., 1991. A study on the genesis of the Ag-Pb-Zn deposit in Laochang, Lancang, Yunnan. J. Guilin Coll. Geol. 11, 245–252 (in Chinese with English abstract).

Yamamoto, M., 1976. Relationship between Se/S and sulfur isotope ratios of hydrothermal sulfide minerals. Miner. Deposita 11, 197–209.

Yang, F., 2014. The Superimposed Metallogenic System and Metallogenic Model of the Laochang Polymetallic Deposits. Kunming University of Science and Technology, pp. 1–190 (in Chinese with English abstract).

Ye, Q.T., Hu, Y.Z., Yang, Y.Q., 1992. The Geochemical Background Character and Mineralization of Au-Ag-Pb-Zn in Sanjiang. Geological Publishing House, Beijing (in Chinese).

Yin, A., Harrison, T.M., 2000. Geologic evolution of the Himalayan-Tibetan orogen. Annu. Rev. Earth Planet. Sci. 28, 211–280.

Zaw, K., Peters, S.G., Cromie, P., Burrett, C., Hou, Z., 2007. Nature, diversity of deposit types and metallogenic relations of South China. Ore Geol. Rev. 31, 3–47.

Zhang, D., Huang, X.-W., Cui, B., Wang, B.-C., Yin, Y.-F., Wang, J.-R., 2016. Re-Os isotopic and trace element compositions of pyrite and origin of the Cretaceous Jinchang porphyry Cu-Au deposit, Heilongjiang Province, NE China. J. Asian Earth Sci. 129, 67–80.

Zhao, X.Y., Li, F., Yang, F., 2012. Isotopic geochemical evidence of the sources of ore-forming materials for the Laochang deep porphyry Mo(Cu) deposit in Lancang, Yunnan. Acta Petrol. Mineral. 31, 712–722 (in Chinese with English abstract).

Zheng, Y., Zhang, L., Chen, Y.-j., Hollings, P., Chen, H.-y., 2013. Metamorphosed Pb–Zn–(Ag) ores of the Keketale VMS deposit, NW China: evidence from ore textures, fluid inclusions, geochronology and pyrite compositions. Ore Geol. Rev. 54, 167–180.

Zwahlen, C., Cioldi, S., Wagner, T., Rey, R., Heinrich, C., 2014. The porphyry Cu-(Mo-Au) deposit at Altar (Argentina): Tracing gold distribution by vein mapping and LA-ICP-MS mineral analysis. Econ. Geol. 109, 1341–1358.